

Widespread wildfires linked to early Albian Ocean Anoxic Event 1b

Xu, Xiaotao; Shao, Longyi; Eriksson, Kenneth; Zhou, Jiamin; Wang, Dongdong; Hou, Haihai; Hilton, Jason; Wang, Shuai; Lu, Jing; Jones, Timothy

DOI:

[10.1016/j.gloplacha.2022.103858](https://doi.org/10.1016/j.gloplacha.2022.103858)

License:

Creative Commons: Attribution-NonCommercial-NoDerivs (CC BY-NC-ND)

Document Version

Peer reviewed version

Citation for published version (Harvard):

Xu, X, Shao, L, Eriksson, K, Zhou, J, Wang, D, Hou, H, Hilton, J, Wang, S, Lu, J & Jones, T 2022, 'Widespread wildfires linked to early Albian Ocean Anoxic Event 1b: evidence from the Fuxin lacustrine basin, NE China', *Global and Planetary Change*, vol. 215, 103858. <https://doi.org/10.1016/j.gloplacha.2022.103858>

[Link to publication on Research at Birmingham portal](#)

General rights

Unless a licence is specified above, all rights (including copyright and moral rights) in this document are retained by the authors and/or the copyright holders. The express permission of the copyright holder must be obtained for any use of this material other than for purposes permitted by law.

- Users may freely distribute the URL that is used to identify this publication.
- Users may download and/or print one copy of the publication from the University of Birmingham research portal for the purpose of private study or non-commercial research.
- User may use extracts from the document in line with the concept of 'fair dealing' under the Copyright, Designs and Patents Act 1988 (?)
- Users may not further distribute the material nor use it for the purposes of commercial gain.

Where a licence is displayed above, please note the terms and conditions of the licence govern your use of this document.

When citing, please reference the published version.

Take down policy

While the University of Birmingham exercises care and attention in making items available there are rare occasions when an item has been uploaded in error or has been deemed to be commercially or otherwise sensitive.

If you believe that this is the case for this document, please contact UBIRA@lists.bham.ac.uk providing details and we will remove access to the work immediately and investigate.

1 **Widespread wildfires linked to early Albian Ocean Anoxic Event**

2 **1b: Evidence from the Fuxin lacustrine basin, NE China**

3
4 **Xiaotao Xu^{a, b}, Longyi Shao^{a, *}, Kenneth A. Eriksson^c, Jiamin Zhou^a, Dongdong Wang^d,**
5 **Haihai Hou^e, Jason Hilton^f, Shuai Wang^e, Jing Lu^a, Timothy P. Jones^g**

6
7 ^a College of Geoscience and Surveying Engineering, China University of Mining and
8 Technology (Beijing), Beijing 100083, China

9 ^b Shandong Key Laboratory of Depositional Mineralization & Sedimentary Mineral, Shandong
10 University of Science and Technology, Qingdao 266590, China

11 ^c Department of Geosciences, Virginia Tech, Blacksburg, Virginia 24061, USA

12 ^d College of Earth Science and Engineering, Shandong University of Science and Technology,
13 Qingdao 266590, China

14 ^e College of Mining, Liaoning Technical University, Fuxin 123000, China

15 ^f School of Geography, Earth and Environmental Sciences, University of Birmingham,
16 Edgbaston, Birmingham, B15 2TT, UK

17 ^g School of Earth and Environmental Sciences, Cardiff University, Cardiff, CF10, 3YE, Wales,
18 UK

19
20 *** Correspondence author**

21 E-mail address: ShaoL@cumtb.edu.cn

22 23 **Abstract**

24 Wildfires are an important source of disturbances in the Earth's system and are of great
25 significance for understanding the interactions between environmental, atmospheric and
26 vegetation changes over deep time. The early Cretaceous was a "high-fire" interval with
27 frequent and widespread wildfires globally, but the timing and global significance of these
28 wildfire events during this time remain uncertain. We undertook a multi-proxy study
29 evaluating kerogen macerals, inertinite reflectance, and polycyclic aromatic hydrocarbons

30 (PAHs) from mudstones to characterize wildfire activity in the Albian coal-forming Fuxin
31 lacustrine Basin, and correlate these with (i) environmental and floral changes on land, and (ii)
32 well-dated marine events including the early Albian Oceanic Anoxic Event 1b (OAE 1b), to
33 consider their environmental and climatic significance. The presence of high inertinite contents
34 demonstrate that multiple, widespread wildfire events occurred during the early Albian, which
35 are correlated stratigraphically to the Kilian, Paquier and Leenhardt sub-events of the early
36 Albian OAE 1b. Inertinite reflectance values ranging from 0.6% to 3.8%Ro show that wildfires
37 in the early Albian were dominated by ground fires, with a smaller proportion of surface fires
38 and almost no crown fires. Atmospheric oxygen concentration (pO_2) levels, estimated from
39 inertinite contents, attained ~25% during the early Albian, which exceeded the present
40 atmospheric oxygen level of 21% and was able to support sustained combustion. Climatic
41 conditions and frequent wildfire activity in the early Albian might have acted as an important
42 control on vegetation distribution and diversification, which possibly further promoted the
43 evolution of early angiosperms during the early Cretaceous. Wildfire activity resulted in the
44 burning and destruction of both vegetation and soil structure, enhancing the post-fire erosion
45 associated with intensified continental weathering under warmer and more humid conditions
46 during the early Albian OAE 1b interval. These episodes of high wildfire activity correlate
47 with high nutrients and organic matter levels in lakes and thereby contributed to eutrophication
48 and anoxia in lacustrine and in contemporaneous oceanic systems.

49

50 **Keywords**

51 Cretaceous; early Albian; Fuxin Basin; wildfires; inertinite; Ocean Anoxic Event 1b

52

53 **1. Introduction**

54 Wildfires have played an important role in Earth system changes since the Silurian period
55 when land plants first appeared on Earth and profoundly influenced global ecosystem patterns
56 and processes (Glasspool et al., 2004; Glasspool et al., 2015; Lu et al., 2021). Charcoal, as the
57 byproduct of wildfires, is recorded from the late Silurian (~420 Ma) to the present (Scott and
58 Glasspool, 2006) and provides evidence for wildfire events in the rock fossil record (Scott and
59 Glasspool, 2007; Scott, 2010; Shao et al., 2012; Wang et al., 2019a; Wang et al., 2021a).

60 Fusinite and semifusinite, the most frequent members of the inertinite maceral group, are
61 believed to be the product of incomplete combustion from wildfires and were regarded as fossil
62 charcoal in previous studies (e.g., Bustin and Guo, 1999; Scott, 2002). Some maceral formation
63 mechanisms in inertinite, such as macrinite, may be related to fungal and/or bacterial
64 degradation and/or arthropod ingestion and excretion (Hower et al., 2013). Although the origin
65 of inertinite is still under frequent debate, more recent studies have concluded that inertinite is
66 synonymous with charcoal and is almost exclusively considered as the byproduct of wildfires
67 (e.g., Scott and Glasspool, 2007; Diessel, 2010; Glasspool and Scott, 2010; Glasspool et al.,
68 2015). Inertinite is common throughout much of the Cretaceous Period (Diessel, 2010; Wang
69 et al., 2021a), and recent evidence indicates widespread and frequent wildfires occurred during
70 the Cretaceous (Bond and Scott, 2010; Brown et al., 2012; Sender et al., 2014; Moore et al.,
71 2021; Wang et al., 2019b, 2021b). Thus, the Cretaceous has been considered as a “high-fire”
72 world (Brown et al., 2012).

73 Polycyclic Aromatic Hydrocarbons (PAHs) in sediments are a powerful proxy for the
74 identification of wildfire process throughout geologic history (e.g., Grice et al., 2007;
75 Marynowski and Simoneit, 2009; Zakir Hossain et al., 2013; Zhou et al., 2021). Numerous
76 studies have shown that unsubstituted PAHs, mostly consisting of 3–6 rings, can be used to
77 indicate pyrogenic sources from combustion of organic matter (Page et al., 1999; Liu et al.,
78 2005; Denis et al., 2012; Xu Y, et al., 2020a). High levels of PAHs are noted in various
79 Cretaceous successions adding further support to the Cretaceous being a “high fire” interval
80 (Finkelstein et al., 2005; Boudinot and Sepúlveda, 2020).

81 Wildfires respond strongly to atmospheric oxygen concentration (pO_2), and variations in
82 the occurrence and abundance of inertinite in the Earth’s history have been used to estimate
83 pO_2 levels (Jones and Chaloner, 1991; Wildman et al., 2004; Belcher et al., 2010; Glasspool
84 and Scott, 2010; Shao et al., 2012; Glasspool et al., 2015; Hou et al., 2020; Wang et al.,
85 2021a). Related studies have revealed that pO_2 above the present-day level of 21% would
86 enable fuels to burn more frequently, while pO_2 levels below 18.5% would suppress fire
87 frequency (Belcher et al., 2010). Wildfire is a significant evolutionary force that has shaped
88 global biome distribution through geological time, and increased wildfire activity has been
89 linked to the abundance of gymnosperms and the emergence of angiosperms (Bond and Scott,

90 2010; Brown et al., 2012). Conifer forests were abundant throughout the Cretaceous Period
91 (e.g., Harland et al., 2007; Friis et al., 2010) from which wildfires have been hypothesized as
92 opening up Cretaceous forests and promoting the expansion of early angiosperms (Bond and
93 Scott, 2010; Belcher and Hudspith, 2016). Additionally, direct and indirect evidence shows
94 that angiosperms created novel wildfire regimes with positive feedbacks leading to more
95 frequent wildfires, which would have facilitated their further diversification and spread (Bond
96 and Scott, 2010; Belcher and Hudspith, 2016; Belcher et al., 2021).

97 The early Albian Oceanic Anoxic Event 1b (OAE 1b) has been widely identified in
98 multiple marine organic-rich sedimentary successions and carbon isotope excursions
99 (Trabucho Alexandre et al., 2011; Coccioni et al., 2014) that represent major disturbances in
100 the global carbon cycle (Jenkyns, 2010). The phenomenon of increased inertinite contents at
101 the onset of Oceanic Anoxic Events (OAEs) has also been observed (Baker et al., 2017), which
102 has provided evidence for enhanced wildfire activity in terrestrial settings during the OAEs
103 onset. According to the model of Handoh and Lenton (2003), increased organic carbon burial
104 across OAEs would have led to a gradual rise in pO_2 level and an increase in wildfire activity.
105 Wildfires can result in the burning and destruction of land surface vegetation and soil structures
106 (Brown et al. 2012), which increases the erosion potential and the flux of terrestrial organic
107 matter and nutrients into the oceans, contributing to oceanic planktonic blooms and associated
108 anoxic events (Brown et al. 2012; Glasspool et al., 2015; Yan et al., 2019; Xu et al., 2020a).

109 Numerous past studies have focused on sedimentary environments, palaeontology,
110 tectonic evolution and coal accumulation in the Lower Cretaceous continental coal-bearing
111 series of the Fuxin Basin (e.g., Chen et al., 1981; Guo, 1988; Liu et al., 1992; Wang et al.,
112 1998; Zhu et al., 2007; Cai et al., 2011; Xu et al., 2020b), making these continental strata ideal
113 for analyzing palaeoclimate and palaeoenvironmental changes during this time. Nevertheless,
114 few studies have focused on wildfire activity in the Lower Cretaceous, and the possible
115 relationships between wildfires, plant evolution, and anoxic events. In this paper, we conduct
116 analyses of kerogen macerals, inertinite reflectance, PAHs of mudstones from the early
117 Cretaceous Shaihai and Fuxin formations in the Fuxin Basin. Based on these data, we identify
118 wildfire records and wildfire types, and attempt to estimate pO_2 levels from inertinite contents
119 and to speculate on the role of wildfires not only on plant evolution, but also on the early

120 Albian OAE 1b. This is important for linking synchronous environmental changes on land and
121 in the oceans to better understand their relationships with one another.

122

123 **2. Geological setting**

124 The continental Fuxin Basin is located in western Liaoning Province, northeastern China,
125 on the northeastern part of the North China Plate (NCP) (Fig. 1a, b; Zhu et al., 2007). During
126 the Jurassic–Cretaceous, the northeastern NCP was located in a back-arc setting and strongly
127 influenced by subduction of the Palaeo-Pacific Plate (Fig. 1c; e.g., Zhu et al., 2017; Su et al.,
128 2021). The Lower Cretaceous represents a peak period of rifting and magmatism in the
129 northeastern NCP (Wu et al., 2014; Zhu et al., 2017). The Fuxin Basin is a fault-bounded basin
130 that formed from rifting in the late Jurassic to early Cretaceous (Liu et al., 1992; Wang et al.,
131 1998). The basin is bounded by the Lvshan Fault to the east and the Songling Fault to the west
132 (Zhu et al., 2007), and extends from Shala city in the north to the Dalinghe Fault in the south
133 (Fig. 2a). During the early Cretaceous the Fuxin Basin was at a palaeolatitude of ~40–45°N
134 (Zhou et al., 2003; Li and Jiang, 2013).

135 The Lower Cretaceous sedimentary rocks in the Fuxin Basin comprise the Yixian,
136 Jiufotang, Shahai, Fuxin, and Sunjiawan formations from oldest to youngest (Fig. 2b; Wan et
137 al., 2013). In this study, the Shahai and Fuxin formations were selected to investigate
138 continental wildfire records. The Shahai Formation mainly consists of mudstone, sandstone
139 and conglomerate, with minor coal seams developed that were deposited in a continually
140 expanding lacustrine basin (Zhu et al., 2007). From the bottom to the top, the Shahai Formation
141 is subdivided into four members according to their lithological association (Li, 1988). The first
142 and second members are mainly composed of conglomerates and coarse-grained sandstones
143 that formed in an alluvial fan depositional system. The third member predominantly consists of
144 sandstones and coal seams and formed in fan delta and lacustrine depositional systems. The
145 fourth member is composed of thick-bedded black mudstones and fine-grained sandstones and
146 is dominated by lacustrine depositional systems (Fig. 3; Guo, 1988; Zhu et al., 2007; Cai et al.,
147 2011). The Fuxin Formation is predominantly composed of sandstones and mudstones with
148 coal seams. It was deposited in fluvial and swamp sedimentary environments (Fig. 3; Xu et al.,
149 2020b).

150 U-Pb zircon ages of the Yixian Formation from volcanic samples have been dated at 131–
151 119 Ma (Xu et al., 2012; Zhang et al., 2016; Su et al., 2021; Fig. 2). Tuff samples from the
152 Jiufotang Formation have given ages of 121–120 Ma (He et al., 2004; Su et al., 2021; Fig. 2).
153 Zircon U-Pb dating of the tuffaceous claystone near the bottom of the fourth member of the
154 Shahai Formation from the DY-1 borehole (1225.5m) gave an age of 112.6 ± 1.7 Ma (Fig. 3;
155 Xu et al., 2022). This age constrains the fourth member of the Shahai Formation to the early
156 part of the Albian Stage. Basalt samples at the top of the Fuxin Formation have yielded
157 $^{40}\text{Ar}/^{39}\text{Ar}$ ages between 105.5 and 102.2 Ma (Zhu et al. 2004). These isotopic ages demonstrate
158 that the Yixian, Jiufotang, Shahai and Fuxin formations are of Lower Cretaceous age. In China,
159 the Lower Cretaceous is divided into the Jibei, Jehol and Liaoxi regional stratigraphic stages
160 (Wan et al., 2013). Of these, the Liaoxi regional stage includes the Shahai, Fuxin and
161 Sunjiawan formations in ascending stratigraphic order, and contains the Fuxin flora (Fig. 2b).
162 The Fuxin flora is dominated by ferns, Ginkgoales and conifers, with abundant cycads and
163 Equisetales and some angiosperms. It has been divided into three floral assemblages (Deng et
164 al. 2012) in which the composition and diversity of angiosperms increase through the early
165 Cretaceous (Tao et al., 2013). The Shahai Formation contains the *Acanthopteris-Ginkgo*
166 *coriacea* assemblage, while the lower-middle part of the Fuxin Formation contains the
167 *Ruffordia goepperti-Dryopterites* assemblage, and the upper part of the Fuxin Formation
168 contains the *Ctenis lyrata-Chilinia* assemblage (Deng et al. 2012). The ages of all three floral
169 assemblages are Lower Cretaceous (Chen et al., 1988; Deng and Chen, 2001), with the Shahai
170 and Fuxin formations dated as late Aptian to Albian in age based on biostratigraphic and
171 lithostratigraphic correlation (Deng et al., 2012; Xi et al., 2019).

172 Historically, it has been difficult to correlate well-dated marine strata with continental
173 successions. The abundance of radiometric dates from Lower Cretaceous continental strata in
174 the NCP (Fig. 2) provide a framework for its accurate correlation with marine strata. In Lower
175 Cretaceous marine successions, OAE 1b is recognized from the late Aptian to the early Albian
176 (~114.5–110.5 Ma) and is subdivided into four subevents; the uppermost Aptian Jacob, and the
177 lower Albian Kilian, Paquier and Leenhardt sub-events (Coccioni et al., 2014; Li et al., 2016;
178 Matsumoto et al., 2020). The sub-events can be recognized from perturbations of the global
179 carbon cycle (Herrle et al., 2004; Navarro-Ramirez et al., 2015) that can be used for

180 chemostratigraphy and correlation with other areas. The early Albian aged Kilian, Paquier and
181 Leenhardt sub-events are each characterized by distinct negative carbon isotope excursions
182 (Herrle et al., 2004; Friedrich et al., 2005; Coccioni et al., 2014), while the late Aptian aged
183 Jacob sub-event is defined by a weak negative carbon isotope excursion within the second late
184 Aptian positive carbon isotope excursion (Coccioni et al., 2014; Herrle et al., 2015). In the
185 Fuxin Basin, three distinct short-term negative excursions of organic carbon isotopes ($\delta^{13}\text{C}_{\text{org}}$)
186 are recorded during the early Albian and are inferred to represent the Kilian, Paquier and
187 Leenhardt sub-events of the early Albian OAE 1b (Xu et al., 2022).

188

189 **3. Materials and methods**

190 Mudstone samples analyzed in this study were collected from the DY-1 borehole (41° 52'
191 45'' N - 121° 37' 8'' E) in the central part of the Fuxin Basin (Fig. 2a). 54 mudstone samples
192 were collected through the Shahai and Fuxin formations (Fig. 3). All samples were collected
193 and stored in airtight, zip-lock plastic bags to avoid oxidation and contamination. Each
194 mudstone sample was crushed to less than 1 mm diameter and then divided into two parts. One
195 part was used for kerogen extraction (GB/T19144-2010) which was prepared as kerogen thin
196 sections and polished epoxy-bound blocks. Identification of kerogen macerals was determined
197 in thin sections under transmitted and fluorescent light using a Leica DM4500P LED
198 microscope according to the China national standard (SY/T 5125-2014), with at least 300 valid
199 points counted for each sample. Inertinite reflectance was measured on polished blocks using a
200 Leica DM4500P LED reflected light microscope with a $\times 50$ oil immersion objective. For the
201 inertinite reflectance measurements, at least 50 valid points were counted on each polished
202 block. The remaining part of each mudstone sample was further crushed below 200 mesh (74
203 microns) for the analysis of PAHs. Aromatic hydrocarbon fractions were analyzed at the State
204 Key Laboratory of Petroleum Resources and Prospecting at the China University of Petroleum
205 in Beijing. Gas chromatography-mass spectrometry (GC-MS) analyses of the aromatic
206 fractions were performed with an Agilent 7890GC/5975CMS following the test method for
207 biomarkers in sediment and crude oil by GC-MS (GB/T 18606-2017). More details of the
208 analysis method are described by Marynowski and Simoneit (2009) and Kang et al. (2020). For
209 observation of homogenized cell walls, small mudstone fragments with charcoalfied plant

210 fossil fragments were mounted on a standard stub, coated with gold, and then observed under a
211 SU8020 Scanning Electron Microscopy (SEM).

212

213 **4. Results**

214 **4.1 Kerogen maceral compositions**

215 Four types of macerals, including sapropelinite, vitrinite, exinite and inertinite, were
216 observed in the mudstone samples from the Fuxin Basin (Fig. 4). Identification results of
217 kerogen macerals (vol.%, mmf–mineral matter free) are given in Table 1 and Fig. 3. The
218 sapropelinite content varies from 5.1 and 52.2 vol.% with an average of 27.5 vol.%, and under
219 transmitted light microscopy is brownish yellow with flocculent edges (Fig. 4a and 4b).
220 Vitrinite accounts for 43.7 vol.% in average, ranging from 16.6 to 75.3 vol.%. Under
221 transmitted light microscopy, vitrinite is brownish red and does not fluoresce under
222 fluorescence illumination (Fig. 4c and 4d). Exinite is not commonly observed, and ranges
223 between 0 and 24.8 vol.% with an average value of 9.3 vol.%. Exinite mainly consists of
224 spores and pollen grains that are yellowish brown in color, fluoresce under fluorescence
225 illumination and exhibits various monomer forms, such as round, oval and triangular shapes
226 (Fig. 4e-j). Inertinite contents range from 8.3 to 42.5 vol.% with an average of 19.5 vol.%,
227 typically exhibiting shapes including cubic blocks and long strips with black color and silky
228 luster (Fig. 5a-j). Under transmitted light microscopy, inertinite entirely consists of fusinite that
229 are pure black in color, do not fluoresce under fluorescence illumination and occur as long
230 strips or fragmental shapes with sharp and angular edges (Fig. 4k, 4l and 4m). Under reflected
231 light microscopy of polished blocks, inertinites shows a prominent cellular structure or
232 compressed and broken cell walls with relatively high reflectivity (Fig. 6). Under the SEM,
233 inertinite exhibits homogenized (stratified in life) cell walls, while some cell walls are
234 fractured, due to the compression associated with burial (Fig. 7).

235 To simplify the discussion and interpretation of the inertinite results, we subdivided the
236 change trends into four units (Fig. 3) based on their overall composition. Unit A, which
237 developed during the early part of the late Aptian, incorporates the first and second members of
238 the Shahai Formation and is characterized by relatively low inertinite contents between 8.3 and
239 15.8 vol.%, with an average of 11.6 vol.%. Unit B, which developed during the latest Aptian

240 represents the third member of the Shahai Formation, has an increased inertinite content that
241 varies from 8.4 to 20.3 vol.%, with an average of 12.9 vol.%. Unit C, which developed during
242 the early Albian defines the fourth member of the Shahai Formation, is characterized by high
243 inertinite contents that range from 14 to 42.5 vol.%. The average content of inertinite in the
244 early Albian is 24.6 vol.% and is higher than that of the other three units. Unit D, which
245 developed during the middle and late Albian defines the Fuxin Formation, is characterized by
246 inertinite contents that range from 8.7 to 17.4 vol.% and display a downward trend.

247

248 **4.2 Inertinite reflectance**

249 The characteristics of inertinite reflectance from all mudstone samples are summarized in
250 Table 1. Units A, B and C are characterized by relatively high values of inertinite reflectance
251 ranging from 1.0–4.3%Ro, 0.8–3.4%Ro, and 0.6–3.8%Ro, respectively. Unit D is characterized
252 by inertinite reflectance values that range from 0.8% to 2.6%Ro and display a decreasing trend
253 upwards. Unit A contains a high proportion (89%) of inertinite with reflectance values between
254 1.8 and 3.5%Ro. In Unit B, most (69%) inertinite contents have reflectance values between 1.8
255 and 3.5%Ro, while 31% of inertinite contents have low reflectance values less than 1.8%Ro.
256 Unit C comprises a proportion (35.5%) of inertinite reflectance between 1.8% and 3.5%Ro and
257 a relatively high proportion (64.3%) of inertinite reflectance less than 1.8%Ro. In Unit D, most
258 (81%) inertinite contents have reflectance values less than 1.8%Ro.

259

260 **4.3 PAHs compounds**

261 A total number of 18 PAHs were detected from ten selected mudstone samples (Fig. 8 and
262 Table 2). The major PAHs compounds identified in all samples are I-Naphthalene, II-Fluorene,
263 III-Biphenyl, IV-Dibenzothiophene, V-Dibenzofuran, VI-Phenanthrene, VII-Anthracene, VIII-
264 Retene, IX-Fluoranthene, X-Benzo(a)fluorine, XI-Benzo(b)fluorine, XII-Pyrene, XIII-
265 Benz(a)anthracene, XIV-Chrysene, XV-Benzofluoranthenes, XVI-Benzo(e)pyrene, XVII-
266 Benzo(a)pyrene, and XVIII-Perylene with more or less intense methyl derivatives of the
267 respective compounds. Quantitative analyses of PAHs show that total concentrations vary from
268 0.081 to 3.846 $\mu\text{g/g}$ mudstone with an average of 1.836 $\mu\text{g/g}$ mudstone (Table 2). Vertically
269 through the succession, the PAHs compounds of Unit C are higher than those of the other three

270 units. In ten mudstone samples (Table 2), the high-molecular-weight of PAHs (5-ring) are
271 identified, such as XVI-Benzo(e)pyrene (0.0004–0.1598 µg/g mudstone), XVII-
272 Benzo(a)pyrene (0.0004–0.3 µg/g mudstone), and XVIII-Perylene (0–0.1878 µg/g mudstone).

273

274 **5. Discussion**

275 **5.1 Evidence of wildfire**

276 Evidence of wildfire is provided by analysis of inertinite (charcoal) and PAHs through the
277 studied section.

278

279 5.1.1 Organic petrographic evidence of wildfire

280 Charcoal, the byproduct of wildfires, provides valuable information on the historical
281 occurrence of wildfires (Scott and Glasspool, 2006; Glasspool and Scott, 2010). Inertinite is
282 widely recognized as a synonym for charcoal and is widely accepted as direct evidence of
283 wildfires in geological deep time (Scott and Glasspool, 2007). Although inertinite may
284 originate from multiple paths (e.g., wildfires and degradation of organic matter), observations
285 on modern charcoal deposits and experimental charring studies indicate that inertinite is
286 formed almost exclusively as a product of wildfires (Jones et al., 1991; Jones, 1994; Scott and
287 Glasspool, 2007).

288 Abundant charcoal particles from several microns to several centimeters were observed in
289 hand specimens, in transmitted and reflected light microscopy and under the SEM (Figs. 4, 5, 6
290 and 7). These macroscopic and microscopic features are consistent with the characteristics of
291 charcoal described by Scott (2010). In the study area, relative inertinite contents (8.3–42.5
292 vol.%) (Table 1) are very similar to relative inertinite values (mostly 10–45 vol.%) in coals
293 from the Lower Cretaceous Erlian, Hailar, and Sanjiang basins in northeastern China (Wang et
294 al., 2019b). Inertinite contents in Unit C are significantly higher than those in the other three
295 units (Fig. 3). This observation provides evidence for an elevated wildfire activity during the
296 early Albian interval. The vertical variation of inertinite abundances in this study (Fig. 3)
297 indicates that wildfires were widespread and frequent in northeastern China during the Lower
298 Cretaceous, which is consistent with the interpretation of Lower Cretaceous “high-fire”
299 conditions especially during the early Albian (Bond and Scott 2010; Diessel, 2010; Brown et

300 al. 2012).

301

302 5.1.2 PAHs evidence of wildfire

303 PAHs are a class of compounds consisting of two or more benzene rings fused in a linear,
304 angular, or clustered arrangement (Chefetz et al., 2000). PAHs originate from two main sources
305 in sedimentary strata, including incomplete combustion of fossil fuels such as coal and
306 petroleum, and other organic matter such as wood (Thompson et al., 2017), as well as
307 degradation of organic matter by microorganisms during diagenesis (Zakir Hossain et al., 2013;
308 Meng et al., 2019). PAHs from pyrogenic sources (combustion of organic matter) mainly
309 consist of 3–6 ring PAHs, which are distinguished by high abundances of unsubstituted
310 compounds (Page et al., 1999; Liu et al., 2005; Denis et al., 2012; Xu et al., 2020c).

311 Unsubstituted PAHs have been extensively regarded as wildfire indicators in sedimentary rocks
312 due to their pyrolytic origin (Liu et al., 2005; Grice et al., 2007; Marynowski and Simoneit,
313 2009; Zakir Hossain et al., 2013). However, the abundance of PAHs is likely to be affected by
314 the thermal history of a basin, which should be seriously considered before interpreting the
315 source of PAHs (Murchison and Raymond, 1989; Jiang et al., 1998; Zhang et al., 2020).

316 Because of the influence of diabase intrusion on the sedimentary strata at the bottom of the
317 Shahai Formation (Zhang et al., 2003; Zhu et al., 2007), the relatively high abundance of PAHs
318 in units A and B might be considered to be the result of rapid heating of organic material by
319 magmatic intrusions (Murchison and Raymond, 1989). In the study area, high-molecular-
320 weight PAHs (3–5 ring) were identified, whereas the PAHs with 6-rings were not found. The
321 occurrence of pyrogenic PAHs indicates that a wide range of wildfires occurred in the Fuxin
322 Basin during the Lower Cretaceous, and the abundance of 3–5 ring PAHs indicates that
323 wildfire activity in Unit C was more intense and frequent than for the other three units.

324 Fluoranthene, pyrene, benz[a]anthracene, benzofluoranthenes, benzo[e]pyrene,
325 benzo[a]pyrene, indeno[1,2,3-cd]pyrene, benzo[ghi]perylene and coronene are commonly
326 considered to be primarily of combustion origin (Zakir Hossain et al., 2013). The higher the
327 number of aromatic rings, the stronger the antioxidant ability of PAHs (Xu et al., 2020c).
328 Studies show that benzo[e]pyrene is highly resistant to oxidation processes (Marynowski et al.,
329 2011) and is the most stable PAH among the 5-ring PAHs (Jiang et al., 1998; Sullivan et al.,

330 1989). The occurrence of PAHs with 5-rings in this study (Fig. 8) also indicates that a wide
331 range of wildfires occurred in the Lower Cretaceous Fuxin Basin. PAH compounds show the
332 different aromatic rings at different combustion temperatures (Zakir Hossain et al., 2013). The
333 high abundances of high-molecular-weight PAHs represent a relatively high combustion
334 temperature, which can provide information on wildfire intensity (Finkelstein et al., 2005;
335 Denis et al., 2012; Zakir Hossain et al., 2013). In the study area, the relatively high abundance
336 of PAHs with 5-rings (benzo[e]pyrene, benzo[a]pyrene and perylene) in Unit C during the
337 early Albian mostly shows high wildfire intensity.

338

339 **5.2 Wildfire types inferred from inertinite reflectance**

340 Inertinites from wildfire activity show a range of reflectance values which are directly
341 related to fire type and temperature (Scott and Jones, 1994; Jasper et al., 2016). Experimental
342 data have demonstrated that high reflectance of inertinite may be the result of increasing
343 temperature during wildfire activity (Jones et al., 1991; Scott and Glasspool, 2007). Although
344 there is no absolute linear relationship between inertinite reflectance and burning temperature,
345 a correlation has been expressed by a linear regression equation derived by Jones (1997): $T =$
346 $184.10 + 117.76 \times \%Ro$ ($r^2 = 0.91$). Where T is the burning temperature and %Ro is the
347 measured inertinite reflectance.

348 Based on experimental data, the ranges of inertinite reflectance for units A, B, C and D are
349 1.0–4.3%Ro, 0.8–3.4%Ro, 0.6–3.8%Ro and 0.8–2.6%Ro, respectively. According to the above
350 equation, the corresponding temperature ranges of inertinite formation are 303.4–696.2 °C,
351 275–589.7 °C, 255–626.8 °C and 278.7–485.7 °C, respectively. Wildfires can be grouped into
352 three types by different burning temperatures, namely, ground fire, surface fire and crown fire
353 (Scott and Jones, 1994; Petersen and Lindström, 2012; Wang et al., 2019b). Ground fires that
354 burn organic material below the litter, generally produce maximum temperatures around 400
355 °C, while surface fires that burn litter and herbaceous and shrubby plants, can reach
356 temperatures around 600 °C. Crown fires typically burn canopies of trees and larger shrubs,
357 which can produce intense heat with temperatures of 800 °C or higher (Scott and Jones, 1994;
358 Petersen and Lindström, 2012; Wang et al., 2019b). In the study area, mudstone samples in
359 units A and B have seemingly circumvented the normal thermal history, with the increase of

360 inertinite reflectance being caused by rapid heating in an environment of magmatic intrusive
361 activity (Murchison and Raymond, 1989). Therefore, units A and B we abandoned for analysis
362 of inertinite reflectance, burning temperature and wildfire type. Although the range of the
363 inertinite reflectance values in Unit C is wide, inertinite with low reflectance values between
364 0.6 and 1.8%Ro accounts for 64.3% of the inertinite content of Unit C. These inertinites have
365 low burning temperatures between 255 and 400 °C, indicating that they are predominantly
366 derived from ground fires (Petersen and Lindström, 2012; Fig. 10). In addition, inertinite with
367 reflectance values between 1.8 and 3.5%Ro accounts for 35.5% of the total inertinite
368 population in Unit C. Their formation temperatures are between 400 and 600 °C, inferring
369 relatively high temperature surface fires (Petersen and Lindström, 2012; Fig. 10). According to
370 Jones (1996) and Scott (2010), the cell walls of inertinite become homogenized above a
371 temperature of 300–325 °C. In Unit C, the inertinite observed under SEM shows homogenized
372 cell walls (Fig. 7), indicating that the burning temperature of wildfire was higher than 300–
373 325 °C. In Unit D, the proportion of inertinite with reflectance values less than 1.8%Ro
374 increases to 81%, while inertinite with reflectance values between 1.8 and 3.5%Ro accounts for
375 19% of the inertinite population of Unit D. These results indicate a decrease in burning
376 temperatures though time in Unit D.

377

378 **5.3 Atmospheric oxygen levels estimated from inertinite contents**

379 Atmospheric oxygen concentration (pO_2) varied dramatically during the Mesozoic
380 (Belcher and McElwain, 2008; Belcher et al., 2010; Mills et al., 2016). Based on models,
381 elevated pO_2 levels have been proposed globally during the Albian (Bergman, 2004; Glasspool
382 and Scott, 2010; Wang et al., 2019b) with a maximum value up to 29% (Glasspool and Scott,
383 2010), significantly higher than present-day 21% concentration (Belcher and McElwain, 2008;
384 Belcher et al., 2010). Berner (2009) predicted pO_2 levels below present-day values until the
385 Albian, thereafter, rising above 21%. Oxygen plays an important role in the occurrence of
386 wildfires and the formation of inertinite (Scott, 2010; Shao et al., 2012; Glasspool et al., 2015;
387 Yan et al., 2019). Experimental data reveal that fire activity would be entirely switched off
388 below pO_2 levels of 16%, greatly suppressed below pO_2 levels of 18.5%, and rapidly enhanced
389 between pO_2 levels of 19–22% (Belcher et al., 2010). If pO_2 significantly exceeded 25%, fire

390 frequencies would have been widespread and even globally in aerial extent (Wildman et al.,
391 2004; Belcher et al., 2010). Previous studies considered that inertinite contents in the
392 sedimentary record could be used to infer atmospheric pO_2 levels (e.g., Scott and Glasspool,
393 2007; Glasspool and Scott, 2010).

394 Glasspool and Scott (2010) and Glasspool et al. (2015) compiled a large database on
395 inertinite contents of coals from different geological periods, and then proposed an inertinite to
396 pO_2 calibration curve. Although this model is based on inertinites found in coals, the relative
397 proportion of the inertinite in the kerogens contained in the mudstones may also give an
398 approximation on the atmospheric oxygen level (Liu et al., 2020). In this study, the relative
399 inertinite contents with an average of 24.6 vol.% from all mudstone samples in Unit C would
400 indicate a pO_2 level of ~25% during the early Albian based on the model of Glasspool et al.
401 (2015) (Fig. 11). The relative content of inertinites in contemporaneous coals of the Fuxin
402 Basin ranged from 12% to 19% (Yang, 1996), and these inertinite contents would give a pO_2
403 level between approximately 23% to 24%. In addition, the pO_2 level estimated from the
404 inertinite contents in the Albian coals of other regions in NE China is around 25.3% (Wang et
405 al., 2019b). The results from coals and mudstones are very similar, and are in accordance with
406 the models of Bergman et al. (2004), Arvidson et al. (2006) and Glasspool and Scott (2010)
407 that estimated pO_2 levels in the early Albian atmosphere were around 25%. As a result, pO_2
408 level may be calculated from relative inertinite contents in mudstone, nevertheless, it needs to
409 be used with caution. From this it can be interpreted that pO_2 levels during the early Albian
410 were much higher than the minimum needed for sustained combustion, and even reached a
411 situation where fires become common. The high pO_2 levels would have led to greatly increased
412 plant flammability, which is consistent with a global record of widespread wildfires during the
413 Lower Cretaceous (Belcher et al., 2010; Diessel, 2010; Wang et al., 2021a; Wang et al., 2019b,
414 2020b).

415

416 **5.4 Contemporaneous wildfires and the evolution of early angiosperms**

417 A growing body of fossil evidence documents angiosperms first evolved in the Lower
418 Cretaceous and subsequently underwent a rapid radiation to gain ecological dominance by the
419 Upper Cretaceous (e.g., Bond and Scott, 2010; Friis et al., 2010; Brown et al., 2012; Coiro et

420 al. 2019). The oldest recognized angiosperms from the megafossil record come from the
421 Barremian aged Yixian Formation (Friis et al., 2010) from the North China Plate. However,
422 while the megafossil record of Cretaceous angiosperms is often scant, records of their
423 distinctive pollen demonstrate that the group first appeared in the Barremian at low
424 paleolatitudes and diversified and spread into higher northern and southern paleolatitudes
425 (Couper, 1958; Coiro et al., 2019). The earliest angiosperms appeared in the middle
426 paleolatitudes during the Albian noted by the presence of pollen genera including
427 *Cupuliferoideaepollenites*, *Fraxinoipollenites*, *Phimopollenites*, *Rousea* and *Tricolpites*
428 (Korasidis et al., 2016), and reached high-latitude Arctic area during the Cenomanian including
429 the pollen genera *Tricolpites* sp. and *Retitricolpites* sp. (Brenner, 1976; Galloway et al., 2012;
430 Coiro et al. 2019).

431 In the North China Plate, Lower Cretaceous continental strata are widely-developed and
432 contain abundant palynomorphs and excellently preserved angiosperm macrofossils which
433 have been used for biostratigraphy and to explore early angiosperm evolution. Lower
434 Cretaceous angiosperm pollen from the North China Plate has been subdivided into five
435 distinct stages from the Barremian, Aptian, early and middle Albian, late Albian, and latest
436 Albian–Cenomanian (Song, 1986). In the Barremian, the monosulcate angiosperm pollen
437 *Clavatipollenites* began to appear in low numbers. During the Aptian, tricolpate angiosperm
438 pollen appeared alongside *Clavatipollenites* but was relatively monotonous morphologically,
439 with angiosperm pollen comprising approximately 5% of Aptian palynofloral assemblage
440 (Song, 1986). In the early and middle Albian, tricolpate pollen types diversified markedly and
441 included more complex forms, and the proportion of angiosperm pollen rose to approximately
442 10%. In the late Albian, tricolporate angiosperm pollen first appeared, with the proportion of
443 the angiosperm pollen in palynofloras remaining at approximately 10%. The latest Albian–
444 Cenomanian palynofloras are marked by the first appearance of oblate tricolporate and
445 triplicate angiosperm pollens and the proportion of angiosperm pollen in palynofloras at this
446 time exceeding 10% (Song, 1986). These five floral stages clearly show the diversification and
447 rise in abundance of angiosperm pollen through the North China Plate during the Lower
448 Cretaceous.

449 Looking more locally at the study area in western Liaoning Province, the Lower

450 Cretaceous has previously been divided into the Jibei, Jehol and Liaoxi regional stratigraphic
451 stages (Wan et al., 2013; Fig. 2). Of these the Barremian–lower Aptian aged Jehol stage
452 corresponds to the Yixian and Jiufotang formations and includes the stratigraphically oldest
453 angiosperm megafossils (Friis et al., 2010) including *Archaeofructus sinensis* and *Sinocarpus*
454 *decussatus* (Sun et al., 1998, 2002; Leng and Friis, 2003; Zhou et al., 2003; Hilton and
455 Bateman, 2006). The upper Aptian-Albian aged Liaoxi regional stage corresponds to the
456 Shahai, Fuxin and Sunjiawan formations in ascending order (Fig. 2). The Shahai and Fuxin
457 formations contain the Fuxin flora that is dominated by ferns, Ginkgoales and conifers with
458 abundant cycads and Equisetales and occasional angiosperms (Deng et al., 2012; Wan et al.,
459 2013). However, despite the megaf flora of the Shahai and Fuxin formations being similar, the
460 *Cicatricosisporites-Pinuspollenites-Classopollis* palynological assemblage in the Shahai
461 Formation contains typical tricolpate angiosperm pollen including *Tricolpites* and
462 *Tricolpopollenites* (Tao et al., 2013), while angiosperm pollen is abundant in the
463 *Cicatricosisporites-Laevigatosporites-Piceapollenites* palynological assemblage in the lower
464 part of the Fuxin Formation (Tao et al., 2013). Angiosperms with complex reticulate leaf
465 venation including *Asiatifolium elegans*, *Chengzihella obovata*, *Jixia pinnatipartita*, *Shenkuoia*
466 *claoneura* and *Rogersia lanceolate* (Sun et al., 1992) occur in the *Ruffordia goepperti-*
467 *Dryopterites* assemblage from the lower-middle part of the Fuxin Formation (Deng et al.
468 2012). The upper part of the Fuxin Formation contains the *Ctenis lyrata-Chilinia* assemblage
469 (Chen et al. 1988) in which angiosperms are relatively abundant and include *Populus* sp.,
470 *Vitiphyllum* sp. and *Trochodendroides* sp. (Deng et al. 2012). Finally, in the Sunjiawan
471 Formation angiosperm pollen became a very common component *Appendicisporites-*
472 *Laevigatosporites* assemblage (Tao et al., 2013). To summarize, the abundance and diversity of
473 angiosperms show a distinct increase from the Yixian Formation to the Sunjiawan Formation
474 during the early Cretaceous in the western Liaoning region.

475 Wildfires have existed as a significant evolutionary force that may have affected the
476 nature of the vegetation itself (Bond and Keeley, 2005; Brown et al., 2012). Many plants have
477 acquired adaptive traits that enable them to cope with fire and reproduce in fire-prone
478 ecosystems (Bond and Scott, 2010; Brown et al., 2012; Belcher et al., 2021). Furthermore,
479 previous studies have suggested that the spread and diversification of angiosperms in the

480 Cretaceous was facilitated by fire regimes (e.g., Bond and Scott, 2010; Friis et al., 2010;
481 Brown et al., 2012). It is especially noteworthy that the earliest known fossil flowers are
482 preserved as charcoalfied mesofossils (e.g., Friis et al., 2010), further emphasizing the
483 relationship of angiosperms with fire. The earliest angiosperms were weedy plants
484 characterized by small herbaceous or shrubby habits with little wood that formed the
485 understory and ground cover (Friis et al., 2010; Royer et al., 2010; Brown et al., 2012). Brown
486 et al. (2012) proposed that herbaceous plants may allow surface fires to burn rapidly. In the
487 study area, 35.5% of inertinite content of the early Albian have experienced relatively high
488 burning temperature between 400 and 600 °C, indicating that they are mainly derived from
489 surface fires. This type of wildfire may have had little effect on soils such that plant roots and
490 seed banks may not have been killed, allowing for rapid regrowth of vegetation and especially
491 herbaceous and shrubby plants following rainfall (Brown et al., 2012). Highly productive
492 weedy angiosperms favour rapid fuel accumulation, which may promote shorter fire cycles
493 under suitable physical preconditions (Bond and Scott, 2010). Frequent Cretaceous wildfires
494 could open up adjacent closed environments and create open sunlit habitats favorable to the
495 expansion of early angiosperms (e.g., Berendse and Scheffer, 2009; Bond and Scott, 2010;
496 Belcher et al., 2021).

497 In the Lower Cretaceous of northeast China, the Fuxin flora from the Shahai and Fuxin
498 formations provided an appropriate source of fuel for wildfires. The spores and pollen grains
499 (Fig. 4e-j) and plant fossil fragments (Fig. 5k and 5l) observed in the early Albian Fuxin Basin
500 also provide evidence for the existence of ferns, conifers and cycads characteristic of the Fuxin
501 Flora. Angiosperms played an increasingly important role in Lower Cretaceous floras in NE
502 China from the Barremian onwards increasing in abundance and diversity through time. The
503 widespread wildfires in the Fuxin Basin during the early Albian coincide with the suggestion
504 that wildfires may have played an important role in promoting the spread and diversification of
505 early angiosperms in this region. In particular, we speculate that frequent surface fires could be
506 conducive to the rapid recovery of the early low-stature angiosperms after burns during the
507 early Albian.

508 Huang et al. (2007) proposed that elevated atmospheric CO₂ levels increases
509 photosynthetic rates and rising *p*CO₂ has a positive effect on plant growth due to increasing

510 availability of carbon. Moreover, enhanced leaf vein densities in the evolution of early
511 angiosperms also potentially increased maximum photosynthetic rates (Brodribb and Field,
512 2010). Elevated $p\text{CO}_2$ levels in the early Albian (Haworth et al., 2005; Hong and Lee, 2012;
513 Sun et al. 2016; Barral et al., 2017; Xu et al., 2022) and high leaf vein densities during the
514 Lower Cretaceous (Field et al., 2011) would have led to an increase in primary productivity,
515 and consequently, greater fuel loads (He et al., 2018). Rapid accumulation of vegetation with
516 high productivity and rapid recovery in the Lower Cretaceous would have provided an ample
517 fuel source for the frequent occurrence of wildfires under high $p\text{O}_2$ levels, which further
518 supports suggestions of a link between wildfires and the spread of early angiosperms.

519

520 **5.5 Continental wildfires linked to the early Albian OAE 1b**

521 OAE 1b is characterized by several short-term perturbations of the global carbon cycle
522 and multiple black mudstone horizons with relatively enhanced organic carbon contents
523 (Trabucho Alexandre et al., 2011). Stratigraphically, OAE 1b spans the late Aptian to early
524 Albian (~110.5–114.5 Ma) and each perturbation corresponds to one of the four sub-events
525 comprising the uppermost Aptian Jacob sub-event, and the lower Albian Kilian, Paquier and
526 Leenhardt sub-events (Coccioni et al., 2014; Li et al., 2016; Matsumoto et al. 2020).

527

528 **5.5.1 Recognition of the Jacob sub-event**

529 The Jacob sub-event is the first organic-rich expression during OAE 1b (Coccioni et al.,
530 2014; Matsumoto et al. 2020). In western Tethys, the Jacob sub-event is ~75 cm thick with a
531 TOC content up to 2.5–8% (Herrle 2002; Heimhofer et al. 2006; Coccioni et al., 2014;
532 Sabatino et al., 2015; Matsumoto et al. 2020). The Jacob sub-event is characterized by a weak
533 negative carbon isotope shift within the second late Aptian positive carbon isotope excursion
534 (Coccioni et al., 2014; Herrle et al., 2015). Matsumoto et al. (2020) conducted a comparative
535 analysis of the negative $\delta^{13}\text{C}_{\text{carb}}$ excursion of the Jacob sub-event in western Tethys and the
536 Pacific Ocean, indicating that it is marked by a weak negative $\delta^{13}\text{C}_{\text{carb}}$ shift of ~0.7‰ in
537 western Tethys (Coccioni et al., 2014; Fig. 9).

538 In the study area, the Aptian/Albian boundary was placed at the boundary between Unit B
539 and Unit C corresponding with an age greater than 112.6 ± 1.7 Ma according to zircon U-Pb

540 dating analyses (Fig. 9; Xu et al., 2022), constraining Unit B to the latest Aptian approximately.
541 In the latest Aptian Fuxin Basin, a weak negative $\delta^{13}\text{C}_{\text{org}}$ excursion of -22.7‰ occurred in an
542 interval of a positive $\delta^{13}\text{C}_{\text{org}}$ excursion near the Aptian/Albian boundary. The peak value of the
543 negative $\delta^{13}\text{C}_{\text{org}}$ shift corresponds to a relatively high TOC value up to 1.1%. From this we
544 interpret that the slight negative $\delta^{13}\text{C}_{\text{org}}$ excursion below the Aptian/Albian boundary may
545 represent the Jacob sub-event (Fig. 9).

546

547 5.5.2 Recognition of the Kilian sub-event

548 The Kilian sub-event is the organic-rich expression of the second sub-event of OAE 1b
549 (Coccioni et al., 2014). Most studied successions in western Tethys and eastern North Atlantic
550 show that the thickness of the Kilian sub-event varies between ~38 cm and 80 cm with TOC
551 contents ranging of ~1–5% (e.g., Herrle, 2002; Herrle et al., 2004; Friedrich et al., 2005;
552 Trabucho Alexandre et al., 2011; Coccioni et al., 2014; Sabatino et al., 2015). The Kilian sub-
553 event also exhibits a short-term negative carbon isotope excursion above the high carbon
554 isotope records of the Jacob sub-event (Herrle et al., 2004; Coccioni et al., 2014). In the
555 western Tethys and the eastern Pacific, the Kilian sub-event is characterized by a negative
556 $\delta^{13}\text{C}_{\text{carb}}$ excursion reaching ~1‰ (Sabatino et al., 2015; Matsumoto et al. 2020) and a large
557 negative $\delta^{13}\text{C}_{\text{org}}$ excursion reaching -26.3‰–25.8‰ (Navarro-Ramirez et al., 2015; Sabatino et
558 al., 2015). In the eastern North Atlantic (DSDP Site 545, Mazagan Plateau), the Kilian sub-
559 event shows a distinct negative carbon isotope excursion ranging from ~2‰ prior to the
560 organic-rich interval to an average value of 0.75‰ during the sub-event, and then a gradual
561 return to carbon isotopic values of ~1.2‰ at its termination (e.g., Herrle, 2002; Herrle et al.,
562 2004; Friedrich et al., 2005; Trabucho Alexandre et al., 2011). In terrestrial records close to the
563 western Pacific in southeastern China, the Kilian sub-event is expressed as a negative
564 excursion with an average $\delta^{13}\text{C}_{\text{org}}$ value of -26.1‰ occurring the 44.4–44.7 m interval in the
565 Shipu section and an average $\delta^{13}\text{C}_{\text{org}}$ value of -27.0‰ in the Chong'an section (Hu et al., 2014).

566 In the early Albian Fuxin Basin, from the bottom to the top the first interval of negative
567 $\delta^{13}\text{C}_{\text{org}}$ excursion decreases from -26.1‰ to -27‰, and then back to -25.6‰ (Fig. 9). Amongst
568 these, the peak value of the negative excursion corresponds with high TOC values up to 4.76%
569 (Xu et al., 2022). Carbon isotopic records during the early Albian are the first distinctly

570 negative $\delta^{13}\text{C}_{\text{org}}$ excursion above the top of the positive $\delta^{13}\text{C}_{\text{org}}$ excursion, which coincides with
571 the characteristics of the Kilian sub-event, a short negative excursion above the positive
572 excursion in the carbon isotope record of the Jacob sub-event (Herrle et al., 2004). In addition,
573 the age of the first negative excursion interval is younger than 112.6 ± 1.7 Ma according to the
574 zircon U-Pb dating analysis (Xu et al., 2022), which could be regarded as the Kilian sub-event
575 equivalent.

576

577 5.5.3 Recognition of the Paquier sub-event

578 The Paquier sub-event is the organic-rich expression of the third sub-event of OAE 1b
579 (Coccioni et al., 2014). In western Tethys and western North Atlantic, the Paquier sub-event is
580 0.25–1.63 m thick and has TOC contents up to 8–12.3% (e.g., Herrle, 2002; Huber et al. 2011;
581 Coccioni et al., 2014; Sabatino et al., 2015; Matsumoto et al. 2020). The Paquier sub-event is
582 defined by a negative excursion in both marine carbonate and organic matter carbon isotope
583 records (e.g., Erbacher et al., 2001; Herrle et al., 2004; Tsikos et al., 2004). In Tethys and the
584 eastern Pacific, the Paquier sub-event commences with an abrupt negative $\delta^{13}\text{C}_{\text{carb}}$ shift
585 reaching values as low as -0.68 – -2.2 ‰, whereas $\delta^{13}\text{C}_{\text{org}}$ values exhibit a gradual negative shift
586 reaching -27 ‰ (e.g., Coccioni et al., 2014; Sabatino et al., 2015; Navarro-Ramirez et al., 2015;
587 Li et al., 2016). In terrestrial records of the western Pacific in southeastern China, the Paquier
588 sub-event displays the strongest negative excursion with a $\delta^{13}\text{C}_{\text{org}}$ peak value of -27.8 ‰ in the
589 Shipu section, and an average $\delta^{13}\text{C}_{\text{org}}$ value of -27.9 ‰ in the Chong'an section (Hu et al.,
590 2014). In terrestrial settings close to eastern Tethys in northwestern China, the Paquier event
591 occurs from 142.2 m–166.8 m in the Hanxiagou section from the Jiuquan Basin and exhibits a
592 strong negative $\delta^{13}\text{C}_{\text{org}}$ excursion from -27 ‰ to -21.7 ‰ representing an ~ 5 ‰ change (Zhao et
593 al., 2022).

594 In the study area, the second interval of negative $\delta^{13}\text{C}_{\text{org}}$ shift from the bottom of the early
595 Albian decreases from -24.8 ‰ to -26.2 ‰, followed by a positive $\delta^{13}\text{C}_{\text{org}}$ excursion with $\delta^{13}\text{C}_{\text{org}}$
596 values up to -24.9 ‰ (Fig. 9; Xu et al., 2022). The magnitude of the negative excursion (1.4‰)
597 in the present study closely matches those in terrestrial records (~ 1.5 ‰) from the Paquier sub-
598 event, including evidence from fossil wood in Japan (Ando et al., 2007), palustrine nodules
599 from the USA (Ludvigson et al., 2010), and terrestrial organic matter from southeastern China

600 (Hu et al., 2014). High resolution carbon isotope records from the Vocontian Basin show that
601 the Paquier sub-event follows after the Kilian sub-event and has a carbon isotope record
602 comprising a short negative excursion after a brief recovery above the Kilian sub-event (Fig. 9;
603 Herrle et al., 2004). A similar negative $\delta^{13}\text{C}_{\text{org}}$ excursion in the early Albian Fuxin Basin
604 suggests that it represents the counterpart of the Paquier sub-event.

605

606 5.5.4 Recognition of the Leenhardt sub-event

607 The Leenhardt sub-event is the organic-rich expression of the fourth sub-event of OAE 1b
608 and has been documented in many regions of the world (Coccioni et al., 2014; Navarro-
609 Ramirez et al., 2015; Li et al., 2016). In western Tethys, the Leenhardt sub-event is 29 cm~92
610 cm thick with TOC contents of 0.95–3% (Herrle, 2002; Coccioni et al., 2014; Sabatino et al.,
611 2015). In Tethys and the eastern Pacific, the Leenhardt sub-event is characterized by a negative
612 $\delta^{13}\text{C}_{\text{carb}}$ excursion reaching -0.1‰~1‰ with negative $\delta^{13}\text{C}_{\text{org}}$ excursion values as low as -28‰
613 (Coccioni et al., 2014; Navarro-Ramirez et al., 2015; Li et al., 2016). In terrestrial records close
614 to the western Pacific in southeastern China, the Leenhardt sub-event shows a relatively weak
615 negative $\delta^{13}\text{C}_{\text{org}}$ excursion with an average $\delta^{13}\text{C}_{\text{org}}$ value of -27.6‰ in the Chong'an section
616 (Hu et al., 2014). In terrestrial records near eastern Tethys from northwestern China, $\delta^{13}\text{C}_{\text{org}}$
617 values decrease from -26.1‰ to -22.8‰ in the 228.3 m–236.3 m interval of the Hanxiagou
618 section in the Jiuquan Basin (Zhao et al., 2022).

619 In the early Albian Fuxin Basin, from the bottom to the top, the third interval of negative
620 $\delta^{13}\text{C}_{\text{org}}$ excursion decreases from -25.7‰ to -26.6‰, and then returns back to -25.1‰ at its
621 termination (Xu et al., 2022). The magnitude of the negative excursion (1.5‰) is similar to
622 those in the eastern Pacific Andean Basin (Navarro-Ramirez et al., 2015) and the western North
623 Atlantic (ODP site 1049 off northern Florida, Blake Nose escarpment; Huber et al., 2011), but
624 is higher than those of hemipelagic and platform carbonates in Tethys, such as from the
625 Umbria-Marche Basin (Coccioni et al., 2014) and the Bangbu section in southern Tibet, China
626 (Li et al., 2016). The negative $\delta^{13}\text{C}_{\text{org}}$ excursion with a peak value up to -26.6‰ is comparable
627 to that of terrestrial records close to the western Pacific from southeastern China (Hu et al.,
628 2014) and that of organic matter in the eastern Pacific Andean Basin (Navarro-Ramirez et al.,
629 2015). Therefore, we conclude that this negative $\delta^{13}\text{C}_{\text{org}}$ shift from the early Albian Fuxin Basin

630 most likely represents the Leenhardt sub-event.

631 In the study area, four sharp, short-term negative $\delta^{13}\text{C}_{\text{org}}$ excursions occur during the late
632 Aptian to early Albian and each corresponds with relatively high TOC values. Furthermore,
633 these correlate well stratigraphically with the Jacob, Kilian, Paquier and Leenhardt sub-events
634 of OAE 1b on the basis of zircon U-Pb age and changing trends and magnitudes of carbon
635 isotope excursions. Based on carbon isotope chemostratigraphy, the sub-events of OAE 1b in
636 the Fuxin Basin can therefore be correlated with six representative research cases including
637 western Tethys, eastern Pacific, western North Atlantic and China (Fig. 9). This comparative
638 analysis indicates that OAE 1b has a global signature and is not only expressed in marine
639 settings but also can be recognized from the terrestrial record.

640 In the Fuxin Basin, mudstone samples in units A and B have seemingly circumvented the
641 normal thermal history, because of the influence of diabase intrusion on the sedimentary strata
642 at the bottom of the Shapai Formation (Zhang et al., 2003; Zhu et al., 2007). Therefore, we
643 abandoned the analysis of wildfire events in units A and B. Three short-term increases of
644 inertinite content and inertinite reflectance correspond to three negative $\delta^{13}\text{C}_{\text{org}}$ excursions and
645 relatively high TOC values during the early Albian interval (Fig. 10). In the study area, the
646 resulting estimates of inertinite content and inertinite reflectance provide evidence for
647 enhanced continental wildfires during the Kilian, Paquier and Leenhardt sub-events of the
648 OAE 1b (Fig. 10).

649 The widespread occurrences of wildfires depend on a combination of factors, such as
650 flammable fuel accumulation, atmospheric $p\text{O}_2$ level, moisture content and ignition mechanism
651 (Bond et al. 2010; Glasspool et al., 2015). The lush Fuxin flora in western Liaoning region
652 during the late Albian–Aptian interval (Deng et al. 2012), would have provided an appropriate
653 source of fuel. The relatively humid palaeoclimate in the early Albian (Xu et al., 2020a) would
654 have reduced the likelihood of wildfire. However, the high $p\text{O}_2$ level of ~25% estimated in the
655 early Albian might render vegetation with relatively high moisture more susceptible to
656 combustion (Glasspool et al., 2015). Five potential sources (apart from human activity) of
657 triggering ignition include lightning strikes, volcanic eruptions, meteor strikes, sparks from
658 rock falls and spontaneous combustion (Belcher et al., 2010; Glasspool et al., 2015). Abundant
659 local volcanic eruptions occurred in the western Liaoning region during the Lower Cretaceous

660 (Cai et al., 2010), which may have acted as the main source of ignition for wildfires.

661 Continental wildfires destroy land surface vegetation systems and soil structure, which
662 increase soil erosion by continental chemical weathering and transfer of land materials (e.g.,
663 minerals, plant residues, charcoal and nutrient elements) into lacustrine and marine
664 environments (Algeo and Ingall, 2007; Brown et al. 2012; Glasspool et al., 2015) contributing
665 to eutrophication and anoxia in lacustrine and in contemporaneous oceanic systems (Brown et
666 al. 2012; Yan et al., 2019; Xu et al., 2020a, 2022). In the study area, the high inertinite contents
667 show that wildfires prevailed in northeastern China during the Lower Cretaceous. In addition,
668 the vertical variation patterns of inertinite content and inertinite reflectance indicate short-term
669 increasing trends of wildfire activity during the Kilian, Paquier and Leenhardt sub-events of the
670 Albian OAE 1b (Fig. 10). Chemical weathering indices have been used to quantitatively track
671 secular variation in chemical weathering intensity, with implications for palaeoclimate
672 reconstruction (Nesbitt and Young, 1982; Fedo et al., 1995; Xu et al., 2018; Lu et al., 2020; Xu
673 et al., 2020a; Gao et al., 2021). Various chemical weathering indices were compiled to
674 illuminate the chemical weathering trend in the Fuxin Basin during the Lower Cretaceous,
675 including the Chemical Index of Alteration (CIA; Nesbitt and Young, 1982), Mafic Index of
676 Alteration for Oxidative weathering environments ($MIA_{(O)}$; Babechuk et al., 2014) and
677 Weathering Index of Parker (WIP; Parker, 1970). The degree of chemical weathering
678 calculated using the chemical weathering indices (CIA, WIP and $MIA_{(O)}$) show an increasing
679 trend during the early Albian OAE 1b interval (Xu et al., 2020a). In the study area, sandstones
680 associated with abundant charcoal fragments have been identified in the Fuxin Basin (Fig. 5a
681 and 5c), which probably represents a post-fire erosion deposit. These sandstones contain
682 charcoals and may be related to increased soil erosion after wildfires. As the result of frequent
683 wildfire activity and intensified chemical weathering, abundant nutrients and organic matter
684 may be transported from continents into lakes where nutrients might increase productivity in
685 surface waters. Transported tree trunk fossils were identified in lacustrine environments of the
686 early Albian (Fig. 5b, 5g and 5h) providing evidence that terrestrial plants were flushed into
687 lakes. Many fossil charcoals identified in lacustrine mudstone in the DY-1 borehole (Fig. 5d, 5e
688 and 5f) may also demonstrate that high flux of nutrients and organic matter produced by
689 increasing wildfire activity and chemical weathering were flushed into lakes through surface

690 runoff. Ultimately, decaying organic matter in surface waters, including terrestrial plants and
691 lacustrine plankton, consumed oxygen during downward passage through the water column,
692 which in turn led to anoxia in lakes (Fig. 12). This unit correlates with the early Albian OAE
693 1b, inferring that frequent wildfire activity at this time promoted high nutrient levels and
694 organic matter that were flushed into marine systems, triggering contemporaneous ocean
695 anoxic event. In this context, many organisms gradually died and organic matter was buried
696 and preserved with an expansion of the oxygen-minimum zone. These results support previous
697 work which proposed that increased wildfires activity stimulated eutrophication and anoxia in
698 lakes and oceans and ultimately organic carbon burial (Brown et al., 2012; Yan et al., 2019;
699 Boudinot and Sepúlveda, 2020).

700

701 **6. Conclusions**

702 (1) High levels of inertinite contents and PAHs in mudstone samples provide evidence for
703 widespread wildfires during the early Albian. The main types of wildfires in the early Albian
704 were ground and surface fires, and the frequency of surface fires was high. Inferred pO_2 levels
705 in the early Albian atmosphere, as estimated from inertinite contents, were ~25%, which is
706 much higher than the minimum needed for sustained combustion. Sufficient fuel accumulation
707 and frequent surface fires under high pO_2 levels might have contributed towards the evolution
708 of early angiosperms in Lower Cretaceous environments.

709 (2) Wildfires destroyed vegetation cover and soil structure in the Fuxin Basin during the
710 early Albian, which enhanced post-fire erosion under the conditions of intensified continental
711 weathering. Post-fire erosion and vegetation destruction may have promoted elevated levels of
712 nutrients and organic matter that were flushed into lakes and thereby contributed to
713 eutrophication and anoxia in lacustrine and contemporaneous oceanic systems. These
714 corresponds to the Kilian, Paquier and Leenhardt sub-events of the early Albian OAE 1b and
715 suggest a temporal linkage between terrestrial and marine environmental perturbations.

716

717 **Declaration of Competing Interest**

718 The authors declare that they have no known competing financial interests or personal
719 relationships that could have appeared to influence the work reported in this paper.

720

721 **Acknowledgments**

722 This study was supported by the Yue Qi Scholar Project of China University of Mining
723 and Technology (Beijing), the National Natural Science Foundation of China (41572090;
724 42002128) and Shandong Key Laboratory of Depositional Mineralization & Sedimentary
725 Mineral, Shandong University of Science and Technology (DMSM20190015). We thank the
726 two anonymous reviewers for the insightful and helpful reviews.

727

728 **References**

- 729 Algeo, T.J., Ingall, E., 2007. Sedimentary C_{org} : P ratios, paleocean ventilation, and Phanerozoic
730 atmospheric pO_2 . *Palaeogeogr. Palaeoclimatol. Palaeoecol.* 256 (3–4), 130–155.
731 <https://doi.org/10.1016/j.palaeo.2007.02.029>.
- 732 Ando, A., Kakegawa, T., 2007. Carbon isotope records of terrestrial organic matter and
733 occurrence of planktonic foraminifera from the Albian stage of Hokkaido, Japan: ocean-
734 atmosphere $\delta^{13}C$ trends and chronostratigraphic implications. *Palaios* 22, 417–432.
735 <http://dx.doi.org/10.2110/palo.2005.p05-104r>.
- 736 Arvidson, R.S., Mackenzie, F.T., Guidry, M., 2006. MAGic: A Phanerozoic model for the
737 geochemical cycling of major rock-forming components. *Am. J. Sci.* 306(3), 135–190.
738 <https://doi.org/10.2475/ajs.306.3.135>.
- 739 Babechuk, M.G., Widdowson, M., Kamber, B.S. 2014. Quantifying chemical weathering
740 intensity and trace element release from two contrasting basalt profiles, Deccan Traps,
741 India. *Chem. Geol.* 363, 56–75. <https://doi.org/10.1016/j.chemgeo.2013.10.027>.
- 742 Baker, S.J., Hesselbo, S.P., Lenton, T.M., Duarte, L.V., Belcher, C.M., 2017. Charcoal evidence
743 that rising atmospheric oxygen terminated Early Jurassic ocean anoxia. *Nat. Commun.* 8,
744 15018. <https://doi.org/10.1038/ncomms15018>.
- 745 Barral, A., Gomez, B., Fourel, F., Daviero-Gomez, V., Lécuyer, C., 2017. CO_2 and temperature
746 decoupling at the million-year scale during the Cretaceous Greenhouse. *Sci. Rep.* 7, 8310.
747 <https://doi.org/10.1038/s41598-017-08234-0>.
- 748 Belcher, C.M., McElwain, J.C., 2008. Limits for combustion in low O_2 redefine
749 paleoatmospheric predictions for the Mesozoic. *Science* 321(5893), 1197-200.

750 <https://doi.org/10.1126/science.1160978>.

751 Belcher, C.M., Hudspith, V.A., 2017. Changes to Cretaceous surface fire behaviour influenced
752 the spread of the early angiosperms. *New Phytol.* 213, 1521–1532.
753 <https://doi.org/10.1111/nph.14264>.

754 Belcher, C.M., Mills, B.J.W., Vitali¹, R., Baker¹, S.J., Lenton, T.M., Watson, A.J., 2021. The
755 rise of angiosperms strengthened fire feedbacks and improved the regulation of
756 atmospheric oxygen. *Nat. Commun.* 12, 503. [https://doi.org/10.1038/s41467-020-20772-](https://doi.org/10.1038/s41467-020-20772-2)
757 [2](https://doi.org/10.1038/s41467-020-20772-2).

758 Belcher, C.M., Yearsley, J.M., Hadden, R.M., McElwain, J.C., Rein, G., 2010. Baseline
759 intrinsic flammability of Earth’s ecosystems estimated from paleoatmospheric oxygen
760 over the past 350 million years. *PNAS* 107(52), 22448–22453.
761 <https://doi.org/10.1073/pnas.1011974107>.

762 Berendse, F., Scheffer, M., 2009. The angiosperm radiation revisited, an ecological explanation
763 for Darwin’s ‘abominable mystery’. *Ecol. Lett.* 12, 865–872.
764 <https://doi.org/10.1111/j.1461-0248.2009.01342.x>.

765 Bergman, N.M., 2004. COPSE: A new model of biogeochemical cycling over Phanerozoic
766 time. *Am. J. Sci.* 304(5), 397–437. <https://doi.org/10.2475/ajs.304.5.397>.

767 Berner, R.A., 2009. Phanerozoic atmospheric oxygen: New results using the GEOCARBSULF
768 model. *Am. J. Sci.* 309(7), 603–606. <https://doi.org/10.2475/07.2009.03>.

769 Boudinot, F.G., Sepúlveda, J., 2020. Marine organic carbon burial increased forest fire
770 frequency during Oceanic Anoxic Event 2. *Nat. Geosci.* 13, 693–698.
771 <https://doi.org/10.1038/s41561-020-0633-y>.

772 Bond, W.J., Keeley, J.E., 2005. Fire as a global ‘herbivore’: the ecology and evolution of
773 flammable ecosystems. *Trends Ecol. Evol.* 20(7), 387–394.
774 <https://doi.org/10.1016/j.tree.2005.04.025>.

775 Bond, W.J., Scott, A.C., 2010. Fire and the spread of flowering plants in the Cretaceous. *New*
776 *Phytol.* 188, 1137–1150. <https://doi.org/10.1111/j.1469-8137.2010.03418.x>.

777 Brenner, G.J., 1976. Middle Cretaceous floral provinces and early migrations of angiosperms.
778 In: Beck, C.B. (Ed.), *Origin and Early Evolution of Angiosperms*. Columbia University
779 Press, New York, USA, pp. 23–47.

780 Brodribb, T.J., Feild, T.S., 2010. Leaf hydraulic evolution led a surge in leaf photosynthetic
781 capacity during early angiosperm diversification. *Ecol. Lett.* 13, 175–183.
782 <https://doi.org/10.1111/j.1461-0248.2009.01410.x>.

783 Brown, S.A.E., Scott, A.C., Glasspool, I.J., Collinson, M.E., 2012. Cretaceous wildfires and
784 their impact on the Earth system. *Cretaceous Res.* 36, 162–190.
785 <https://doi.org/10.1016/j.cretres.2012.02.008>.

786 Bustin, R.M., Guo, Y., 1999. Abrupt changes (jumps) in reflectance values and chemical
787 compositions of artificial charcoals and inertinite in coals. *Int. J. Coal Geol.* 38, 237–260.
788 [https://doi.org/10.1016/S0166-5162\(98\)00025-1](https://doi.org/10.1016/S0166-5162(98)00025-1).

789 Cai, H.A., Li, B.F., Shao, L.Y., Xu, D.B., Shao, K., Zhou, Y.Y., 2011. Sedimentary
790 environments and coal accumulation patterns of the Lower Cretaceous Shaihai Formation
791 in Fuxin Basin, Liaoning Province. *J. Palaeogeogr.* 13 (5), 481–491 (in Chinese with
792 English abstract).

793 Cai, H.A., Xu, D.B., Li, B.F., Shao, L.Y., 2010. A study on Early Cretaceous volcanic effusion
794 periods and isotope chronology in western Liaoning. *Coal Geol. Explor.* 22 (12), 1–6 (in
795 Chinese with English abstract).

796 Chefetz, B., Deshmukh, A.P., Hatcher, P.G., Guthrie, E.A., 2000. Pyrene sorption by natural
797 organic matter. *Environ. Sci. Technol.* 34(14), 2925–2930.
798 <https://doi.org/10.1021/es9912877>.

799 Chen, F., Meng, X.Y., Ren, S.Q., Wu, C.L., 1988. The Early Cretaceous flora of Fuxin Basin
800 and Tiefert Basin, Liaoning Province. Geological Publishing House, Beijing, pp. 1–180. (in
801 Chinese).

802 Chen, F., Yang, G.X., Zhou, H.Q., 1981. Early Cretaceous flora in Fuxin Basin, Liaoning
803 Province. *J. Earth Sci. (Chinese Ed.)* 6(2), 39–55. (in Chinese with English abstract).

804 Coccioni, R., Sabatino, N., Frontalini, F., Gardin, S., Sideri, M., Sprovieri, M., 2014. The
805 neglected history of Oceanic Anoxic Event 1b: insights and new data from the Poggio le
806 Guaine section (Umbria-Marche Basin). *Stratigraphy* 11(3–4), 245–282.

807 Coiro, M., Doyle, J.A., Hilton, J., 2019. How deep is the conflict between molecular and fossil
808 evidence on the age of angiosperms? *New Phytol.* 223, 83–89.
809 <https://doi.org/10.1111/nph.15708>.

- 810 Couper, R.A., 1958. British Mesozoic microspores and pollen grains. *Palaeontographica*
811 Abteilung B 103, 75–179.
- 812 Deng, S.H., Chen, F., 2001. The Early Cretaceous Filicopsida from Northeast China.
813 Geological Publishing House, Beijing, pp. 1–249 (in Chinese).
- 814 Deng, S.H., Lu, Y.Z., Fan, R., Li, X., Fang, L.H., Liu, L., 2012. Cretaceous floras and
815 biostratigraphy of China. *J. Stratigr.* 36(2), 241–265.
- 816 Denis, E.H. Toney, J.L., Tarozo, R., Scott Anderson, R., Roach, L.D. Huang, Y.S., 2012.
817 Polycyclic aromatic hydrocarbons (PAHs) in lake sediments record historic fire events:
818 Validation using HPLC-fluorescence detection. *Org. Geochem.* 45, 7–17.
819 <https://doi.org/10.1016/j.orggeochem.2012.01.005>.
- 820 Diessel, C.F.K., 2010. The stratigraphic distribution of inertinite. *Int. J. Coal Geol.* 81, 251–
821 268. <https://doi.org/10.1016/j.coal.2009.04.004>.
- 822 Erbacher, J., Huber, B.T., Norris, R.D., Markey, M., 2001. Increased thermohaline stratification
823 as a possible cause for an ocean anoxic event in the Cretaceous period. *Nature* 409, 325–
824 327. <https://doi.org/10.1038/35053041>.
- 825 Fedo, C.M., Nesbitt, H.W., Young, G.M., 1995. Unravelling the effects of potassium
826 metasomatism in sedimentary rocks and paleosols, with implications for paleoweathering
827 conditions and provenance. *Geology* 23(10), 921–924.
- 828 Feild, T.S., Brodribb, T.J., Iglesias, A., Chatelet, D.S., Baresch, A., Jr., G.R.U., Gomez, B.,
829 Mohr, B.A.R., Coiffard, C., Kvacek, J., Jaramillo, C., 2011. Fossil evidence for
830 Cretaceous escalation in angiosperm leaf vein evolution. *PNAS* 108(20), 8363–8366.
831 <https://doi.org/10.1073/pnas.1014456108>.
- 832 Finkelstein, D.B., Pratt, L.M., Curtin, T.M., Brassell, S.C., 2005. Wildfires and seasonal aridity
833 recorded in Late Cretaceous strata from south-eastern Arizona, USA. *Sedimentology* 52,
834 587–599. <https://doi.org/10.1111/j.1365-3091.2005.00712.x>.
- 835 Friis, E.M., Pedersen, K.R., Crane, P.R., 2010. Cretaceous diversification of angiosperms in the
836 western part of the Iberian Peninsula. *Rev. Palaeobot. Palyno.* 162, 341–361.
837 <https://doi.org/10.1016/j.revpalbo.2009.11.009>.
- 838 Friedrich, O., Nishi, H., Pross, J., Schmiiedl, G., Hemleben, C., 2005. Millennial- to Centennial-
839 Scale Interruptions of the Oceanic Anoxic Event 1b (Early Albian, mid-Cretaceous)

840 Inferred from Benthic Repopulation Events. *Palaios* 20, 64–77.
841 <https://doi.org/10.2110/palo.2003.p03-75>.

842 Gao, Y., Ibarra, D.E., Caves Rügenstein, J.K., Chen, J.Q., Kukla, T., Methner, K., Gao, Y.F.,
843 Huang, H., Lin, Z.P., Zhang, L.M., Xi, D.P., Wu, H.C., Carroll, A.R., Graham, S.A.,
844 Chamberlain, C.P., Wang, C.S., 2021. Terrestrial climate in mid-latitude East Asia from
845 the latest Cretaceous to the earliest Paleogene: A multiproxy record from the Songliao
846 Basin in northeastern China. *Earth-Science Reviews* 216, 103572.
847 <https://doi.org/10.1016/j.earscirev.2021.103572>.

848 Galloway, J.M., Sweet, A.R., Pugh, A., Schröder-Adams, C.J., Swindles, G.T., Haggart, J.W.,
849 Embry, A.F., 2012. Correlating middle Cretaceous palynological records from the
850 Canadian High Arctic based on a section from the Sverdrup Basin and samples from the
851 Eclipse Trough. *Palynology* 36, 277–302. <https://doi.org/10.1080/01916122.2012.670411>.

852 Glasspool, I.J., Edwards, D., Axe, L., 2004. Charcoal in the Silurian as evidence for the earliest
853 wildfire. *Geology* 32(5), 381–383. <https://doi.org/10.1130/G20363.1>.

854 Glasspool, I.J., Scott, A.C., 2010. Phanerozoic concentrations of atmospheric oxygen
855 reconstructed from sedimentary charcoal. *Nat. Geosci.* 3, 627–630.
856 <https://doi.org/10.1038/NGEO923>.

857 Glasspool, I.J., Scott, A.C., Waltham, D., Pronina, N., Shao, L.Y., 2015. The impact of fire on
858 the Late Paleozoic Earth system. *Front. Plant Sci.* 6, 756.
859 <https://doi.org/10.3389/fpls.2015.00756>.

860 Grice, K., Nabbefeld, B., Maslen, E., 2007. Source and significance of selected polycyclic
861 aromatic hydrocarbons in sediments (Hovea-3 well, Perth Basin, Western Australia)
862 spanning the Permian–Triassic boundary. *Org. Geochem.* 38, 1795–1803.
863 <https://doi.org/10.1016/j.orggeochem.2007.07.001>.

864 Guo, Z.Y., 1988. Relationship between alluvial fan-delta depositional system and coal
865 accumulation of Shaihai Formation in Fuxin Basin. *Coal Geol. Explor.* 16(4), 2–7. (in
866 Chinese).

867 Handoh, I.C., Lenton, T.M., 2003. Periodic mid-Cretaceous oceanic anoxic events linked by
868 oscillations of the phosphorus and oxygen biogeochemical cycles. *Global Biogeochem.*
869 *Cy.* 17(4), 1092. <https://doi.org/10.1029/2003GB002039>.

- 870 Harland, M., Francis, J.E., Brentnall, S.J., Beerling, D.J., 2007. Cretaceous (Albian–Aptian)
871 conifer wood from Northern Hemisphere high latitudes: Forest composition and
872 palaeoclimate. *Rev. Palaeobot. Palyno.* 143, 167–196.
873 <https://doi.org/10.1016/j.revpalbo.2006.07.005>.
- 874 Haworth, M., Hesselbo, S.P., McElwain, J.C., Robinson, S.A., Brunt, J.W., 2005. Mid-
875 Cretaceous $p\text{CO}_2$ based on stomata of the extinct conifer *Pseudofrenelopsis*
876 (Cheirolepidiaceae). *Geology* 33(9), 749–752. <https://doi.org/10.1130/G21736.1>.
- 877 He, H.Y., Wang, X.L., Zhou, Z.H., Wang, F., Boven, A., Shi, G.H., Zhu, R.X., 2004. Timing
878 of the Jiufotang Formation (Jehol Group) in Liaoning, northeastern China, and its
879 implications. *Geophys. Res. Lett.* 31, 261–268. <https://doi.org/10.1029/2004GL019790>.
- 880 He, T., Lamont, B.B., 2018. Baptism by fire: the pivotal role of ancient conflagrations in
881 evolution of the Earth’s flora. *Natl. Sci. Rev.* 5, 237–254.
882 <https://doi.org/10.1093/nsr/nwx041>.
- 883 Heimhofer, U., Hochuli, P.A., Herrle, J.O., Weissert, H., 2006. Contrasting origins of Early
884 Cretaceous black shales in the Vocontian basin: Evidence from palynological and
885 calcareous nannofossil records. *Palaeogeogr. Palaeoclimatol. Palaeoecol.* 235, 93–109.
886 <https://doi.org/10.1016/j.palaeo.2005.09.025>.
- 887 Herrle, J.O., 2002. Mid-Cretaceous paleoceanographic and paleoclimatologic implications on
888 black shale formation of the Vocontian Basin and Atlantic: evidence from calcareous
889 nannofossils and stable isotopes. *Tübinger Mikropaläontologische Mitteilungen* 27, 1–
890 114.
- 891 Herrle, J.O., Kößler, P., Friedrich, O., Erlenkeuser, H., Hemleben, C., 2004. High-resolution
892 carbon isotope records of the Aptian to Lower Albian from SE France and the Mazagan
893 Plateau (DSDP Site 545): a stratigraphic tool for paleoceanographic and paleobiologic
894 reconstruction. *Earth Planet Sci. Lett.* 218(1), 149–161. [https://doi.org/10.1016/S0012-821X\(03\)00646-0](https://doi.org/10.1016/S0012-821X(03)00646-0).
- 896 Herrle, J.O., Schroder-Adams, C.J., Davis, W., Pugh, A.T., Galloway, J.M., Fath, J., 2015. Mid-
897 Cretaceous High Arctic stratigraphy, climate, and Oceanic Anoxic Events. *Geology* 43(5),
898 403–406. <https://doi.org/10.1130/G36439.1>.
- 899 Hilton, J., Bateman, R.M., 2006. Pteridosperms are the backbone of seed–plant phylogeny.

900 Journal of the Torrey Botanical Society 133, 119–168. <https://doi.org/10.3159/1095->
901 5674(2006)133[119:PATBOS]2.0.CO;2.

902 Hou, H.H., Shao, L.Y., Tang, Y., Li, Y.N., Liang, G.D., Xin, Y.L., Zhang, J.Q., 2020. Coal seam
903 correlation in terrestrial basins by sequence stratigraphy and its implications for
904 palaeoclimate and palaeoenvironment. *J. Earth Sci.* <https://doi.org/10.1007/s12583-020->
905 1069-4.

906 Hower, J.C., O'Keefe, J.M.K., Wagner, N.J., Dai, S.F., Wang, X.B., Xue, W.F., 2013. An
907 investigation of Wulantuga coal (Cretaceous, Inner Mongolia) macerals: Paleopathology
908 of faunal and fungal invasions into wood and the recognizable clues for their activity. *Int.*
909 *J. Coal Geol.* 114(30), 44–53. <https://doi.org/10.1016/j.coal.2013.04.005>.

910 Hong, S.K., Lee, Y.I., 2012. Evaluation of atmospheric carbon dioxide concentrations during
911 the Cretaceous. *Earth Planet. Sci. Lett.* 327-328, 23–28.
912 <https://doi.org/10.1016/j.epsl.2012.01.014>.

913 Hu, G., Hu, W., Cao, J., Yao, S., Liu, W., Zhou, Z., 2014. Fluctuation of organic carbon
914 isotopes of the Lower Cretaceous in coastal southeastern China: Terrestrial response to the
915 Oceanic Anoxic Events (OAE 1b). *Palaeogeogr. Palaeoclimatol. Palaeoecol.* 399, 352–
916 362. <http://dx.doi.org/10.1016/j.palaeo.2014.01.027>.

917 Huang, J.G., Bergeron, Y., Denneler, B., Berninger, F., Tardif, J., 2007. Response of forest trees
918 to increased atmospheric CO₂. *Crit. Rev. Plant Sci.* 26, 265–283.
919 <https://doi.org/10.1080/07352680701626978>.

920 Huber, B.T., Macleod, K.G., Gröcke, D.R., Kucera, M., 2011. Paleotemperature and
921 paleosalinity inferences and chemostratigraphy across the Aptian/Albian boundary in the
922 subtropical North Atlantic. *Paleoceanography* 26, PA4221.
923 <http://dx.doi.org/10.1029/2011PA002178>.

924 Jasper, A., Agnihotri, D., Tewari, R., Spiekermann, R., Pires, E.F., Rosa, Á.A.S.D., Uhl, D.,
925 2016. Fires in the mire: repeated fire events in Early Permian ‘peat forming’ vegetation of
926 India. *Geol. J.* 52(6), 955-969. <http://dx.doi.org/10.1002/gj.2860>.

927 Jenkyns, H.C., 2010. Geochemistry of oceanic anoxic events. *Geochem. Geophys. Geosy.*
928 11(3), 1–30. <http://dx.doi.org/10.1029/2009GC002788>.

929 Jiang, C., Alexander, R., Kagi, R.I., Murray, A.P., 1998. Polycyclic aromatic hydrocarbons in

930 ancient sediments and their relationships to palaeoclimate. *Org. Geochem.* 29(5-7), 1721–
931 1735. [http://dx.doi.org/10.1016/S0146-6380\(98\)00083-7](http://dx.doi.org/10.1016/S0146-6380(98)00083-7).

932 Jones, T.P., Chaloner, W.G., 1991. Fossil charcoal, its recognition and palaeoatmospheric
933 significance. *Palaeogeogr. Palaeoclimatol. Palaeoecol.* 97(1–2), 39–50.
934 [https://doi.org/10.1016/0031-0182\(91\)90180-Y](https://doi.org/10.1016/0031-0182(91)90180-Y).

935 Jones, T.P., Scott, A.C., Cope, M., 1991. Reflectance measurements and the temperature of
936 formation of modern charcoals and implications for studies of fusain. *Bulletin de la*
937 *Société Géologique de France* 162(2), 193–200.

938 Jones, T.P., 1994. New morphological and chemical evidence supporting a wildfire origin for
939 fusain from comparisons with modern charcoal. In: Collinson, M. and Scott, A.C. (Eds.),
940 *Studies in Palaeobotany and Palynology in Honour of Professor W. G. Chaloner, F.R.S.,*
941 *Special Papers in Palaeontology*, vol. 49. Palaeontological Association, London, pp. 113–
942 123.

943 Jones, T.P., 1996. A fire-related origin for fusain: comparisons with the physicochemical
944 characteristics of laboratory produced charcoal. *Neues Jahrbuch für Geologie und*
945 *Paläontologie - Abhandlungen* 202(2), 159–168.
946 <https://doi.org/10.1127/njgpa/202/1996/159>.

947 Jones, T.P., 1997. Fusain in Late Jurassic sediments from Witch Ground Graben, North Sea,
948 U.K. *Mededelingen Nederlands Instituut voor Toegepaste Geowetenschappen TNO* 58,
949 93–103.

950 Kang, S.L., Shao, L.Y., Qin, L.Z., Li, S.X., Liu, J.S., Shen, W.C., Chen, X.D., Eriksson, K.A.,
951 Zhou, Q.Y., 2020. Hydrocarbon generation potential and depositional setting of Eocene
952 oil-prone coaly source rocks in the Xihu Sag, East China Sea Shelf Basin. *ACS Omega*
953 5(50), 32267–32285. <https://dx.doi.org/10.1021/acsomega.0c04109>.

954 Korasidis, V.A., Wagstaff, B.E., Gallagher, S.J., Duddy, I.R., Tosolini, AMP., Cantrill, D.J.,
955 Norvick, M.S., 2016. Early angiosperm diversification in the Albian of southeast
956 Australia: implications for flowering plant radiation across eastern Gondwana. *Rev.*
957 *Palaeobot. Palyno.* 232: 61–80. <https://doi.org/10.1016/j.revpalbo.2016.04.005>.

958 Leng, Q., Friis, E.M., 2003. *Sinocarpus decussates* gen. et sp. nov., a new angiosperm with
959 basally syncarpous fruits from the Yixian Formation of Northeast China. *Plant Syst. Evol.*

960 241, 77–88.

961 Li, J.H., Jiang, H.F., 2013. Global palaeoplate reconstruction, lithofacies palaeogeography and
962 paleoenvironmental atlas. Geological Publishing House, Beijing, pp. 1–127 (in Chinese).

963 Li, S.T., 1988. Fault basin analysis and coal accumulation. Geological Publishing House,
964 Beijing, pp. 1–367. (in Chinese).

965 Li, X.H., Wei, Y.S., Li, Y.X., Zhang, C.K., 2016. Carbon isotope records of the early Albian
966 oceanic anoxic event (OAE) 1b from eastern Tethys (southern Tibet, China). *Cretaceous*
967 *Res.* 62, 109–121. <https://doi.org/10.1016/j.cretres.2015.08.015>.

968 Liu, J.Y., Wang, S.Y., Yin, J.H., 1992, Petroleum geological character of Fuxin Basin. *Oil Gas*
969 *Geol.* 13(4), 450–457 (in Chinese with English abstract).

970 Liu, G.Q., Zhang, G., Li, X.D., Li, J., Peng, X.Z., Qi, S.H., 2005. Sedimentary record of
971 polycyclic aromatic hydrocarbons in a sediment core from the Pearl River Estuary, South
972 China. *Mar. Pollut. Bull.* 51, 912–921.
973 <https://dx.doi.org/10.1016/j.marpolbul.2005.02.038>.

974 Liu, Z.Y., Selby, D., Hackley, P.C., Jeffrey Over, D., 2020. Evidence of wildfires and elevated
975 atmospheric oxygen at the Frasnian–Famennian boundary in New York (USA):
976 Implications for the Late Devonian mass extinction. *Geol. Soc. Am. Bull.* 132 (9-10),
977 2043–2054. <https://doi.org/10.1130/B35457.1>.

978 Lu, J., Zhou, K., Yang, M.F., Eley, Y., Shao, L.Y., Hilton, J., 2020. Terrestrial organic carbon
979 isotopic composition ($\delta^{13}\text{C}_{\text{org}}$) and environmental perturbations linked to Early Jurassic
980 volcanism: evidence from the Qinghai-Tibet Plateau of China. *Glob. Planet. Chang.* 195,
981 103331. <https://doi.org/10.1016/j.gloplacha.2020.103331>.

982 Lu, M., Ikejiri, T., Lu, Y.H., 2021. A synthesis of the Devonian wildfire record: Implications
983 for paleogeography, fossil flora, and paleoclimate. *Palaeogeogr. Palaeoclimatol.*
984 *Palaeoecol.* 571, 110321. <https://doi.org/10.1016/j.palaeo.2021.110321>.

985 Ludvigson, G.A., Joeckel, R.M., Gonzalez, L.A., Gulbranson, E.L., Rasbury, E.T., Hunt, G.J.,
986 Kirkland, J.I., Madsen, S., 2010. Correlation of Aptian-Albian carbon isotope excursions in
987 continental strata of the Cretaceous foreland basin, eastern Utah, U.S.A. *J. Sed. Res.* 80,
988 955–974. <http://dx.doi.org/10.2110/jsr.2010.086>.

989 Marynowski, L., Kurkiewicz, S., Rakocinski, M., Simoneit, B.R.T., 2011. Effects of

990 weathering on organic matter: I. Changes in molecular composition of extractable organic
991 compounds caused by paleoweathering of a Lower Carboniferous (Tournaisian) marine
992 black shale. *Chem. Geol.* 285, 144–156. <https://dx.doi.org/10.1016/j.chemgeo.2011.04.001>.

993 Marynowski, L., Simoneit, B.R.T., 2009. Widespread upper Triassic to Lower Jurassic wildfire
994 records from Poland: Evidence from charcoal and pyrolytic polycyclic aromatic
995 hydrocarbons. *Palaios* 24, 785–798. <https://dx.doi.org/10.2110/palo.2009.p09-044r>.

996 Matsumoto, H., Kuroda, J., Coccioni, R., Frontalini, F., Sakai, S., Ogawa, N.O., Ohkouchi, N.,
997 2020. Marine Os isotopic evidence for multiple volcanic episodes during Cretaceous
998 Oceanic Anoxic Event 1b. *Sci. Rep.* 10, 12601. [https://doi.org/10.1038/s41598-020-](https://doi.org/10.1038/s41598-020-69505-x)
999 [69505-x](https://doi.org/10.1038/s41598-020-69505-x).

1000 Meng, Y., Liu, X.H., Lu, S.Y., Zhang, T.T., Jin, B.C., Wang, Q., Tang, Z.R., Liu, Y., Guo, X.H.,
1001 Zhou, J.L., Xi, B.D., 2019. A review on occurrence and risk of polycyclic aromatic
1002 hydrocarbons (PAHs) in lakes of China. *Sci. Total Environ.* 651, 2497–2506.
1003 <https://doi.org/10.1016/j.scitotenv.2018.10.162>.

1004 Mills, B.J.W., Belcher, C.M., Lenton, T.M., Newton, R.J., 2016. A modeling case for high
1005 atmospheric oxygen concentrations during the Mesozoic and Cenozoic. *Geology*, 44(12),
1006 1023–1026. <https://doi.org/10.1130/G38231.1>.

1007 Moore, T.A., Moroeng, O.M., Shen, J., Esterle, J.S., Pausch, R.C., 2021. Using carbon isotopes
1008 and organic composition to decipher climate and tectonics in the Early Cretaceous: An
1009 example from the Hailar Basin, Inner Mongolia, China. *Cretaceous Res.* 118, 104674.
1010 <https://doi.org/10.1016/j.cretres.2020.104674>.

1011 Murchison, D.G., Raymond, A.C., 1989. Igneous activity and organic maturation in the
1012 Midland Valley of Scotland. *Int. J. Coal Geol.* 14, 47–82. [https://doi.org/10.1016/0166-](https://doi.org/10.1016/0166-5162(89)90078-5)
1013 [5162\(89\)90078-5](https://doi.org/10.1016/0166-5162(89)90078-5).

1014 Navarro-Ramirez, J.P., Bodin, S., Heimhofer, U., Immenhauser, A., 2015. Record of Albian to
1015 early Cenomanian environmental perturbation in the eastern sub-equatorial Pacific.
1016 *Palaeogeogr. Palaeoclimatol. Palaeoecol.* 423, 122–137.
1017 <http://dx.doi.org/10.1016/j.palaeo.2015.01.025>.

1018 Nesbitt, H.W., Young, G.M., 1982. Early Proterozoic climates and plate motions inferred from
1019 major element chemistry of lutites. *Nature* 299, 715–717.

- 1020 <https://doi.org/10.1038/299715a0>.
- 1021 Oakley, O., Falcon-Lang, H.J., 2009. Morphometric analysis of Cretaceous (Cenomanian)
1022 angiosperm woods from the Czech Republic. *Rev. Palaeobot. Palyno.* 153, 375–385.
1023 <https://doi.org/10.1016/j.revpalbo.2008.10.006>.
- 1024 Page, D.S., Boehm, P.D., Douglas, G.S., Bence, A.E., Burns, W.A., Mankiewicz, P.J., 1999.
1025 Pyrogenic polycyclic aromatic hydrocarbons in sediments record past human activity: A
1026 case study in Prince William Sound, Alaska. *Mar. Pollut. Bull.* 38(4), 247–260.
1027 [https://doi.org/10.1016/S0025-326X\(98\)00142-8](https://doi.org/10.1016/S0025-326X(98)00142-8).
- 1028 Parker, A. 1970. An index of weathering for silicate rocks. *Geol. Mag.* 107(6), 501–504.
1029 <https://doi.org/10.1017/S0016756800058581>.
- 1030 Petersen, H.I., Lindstrom, S., 2012. Synchronous wildfire activity rise and mire deforestation at
1031 the Triassic–Jurassic boundary. *PLOS ONE* 7(10), e47236.
1032 <https://doi.org/10.1371/journal.pone.0047236>.
- 1033 Royer, D.L., Miller, I.M., Peppe, D.J., Hickey, L.J., 2010. Leaf economic traits from fossils
1034 support a weedy habit for early angiosperms. *Am. J. Bot.* 97(3), 438–445.
1035 <https://doi.org/10.3732/ajb.0900290>.
- 1036 Sabatino, N., Coccioni, R., Manta, D.S., Baudin, F., Vallefucio, M., Traina, A., Sprovieri, M.,
1037 2015. High-resolution chemostratigraphy of the late Aptian-early Albian oceanic anoxic
1038 event (OAE 1b) from the Poggio le Guaine section (Umbria–Marche Basin, central Italy).
1039 *Palaeogeogr. Palaeoclimatol. Palaeoecol.* 426, 319–333.
1040 <https://doi.org/10.1016/j.palaeo.2015.03.009>.
- 1041 Scott, A.C., 2002. Coal petrology and the origin of coal macerals: a way ahead? *Int. J. Coal*
1042 *Geol.* 50, 119–134.
- 1043 Scott, A.C., 2010. Charcoal recognition, taphonomy and uses in palaeoenvironmental analysis.
1044 *Palaeogeogr. Palaeoclimatol. Palaeoecol.* 291, 11–39.
1045 <https://doi.org/10.1016/j.palaeo.2009.12.012>.
- 1046 Scott, A.C., Glasspool, I.J., 2006. The diversification of Paleozoic fire systems and fluctuations
1047 in atmospheric oxygen concentration. *PNAS* 103(29), 10861–10865.
1048 <https://doi.org/10.1073/pnas.0604090103>.
- 1049 Scott, A.C., Glasspool, I.J., 2007. Observations and experiments on the origin and formation of

1050 inertinite group macerals. *Int. J. Coal Geol.* 70, 53–66.
1051 <https://doi.org/10.1016/j.coal.2006.02.009>.

1052 Scott, A.C., Jones, T.P., 1994. The nature and influence of fire in Carboniferous ecosystems.
1053 *Palaeogeogr. Palaeoclimatol. Palaeoecol.* 106, 91–112. [https://doi.org/10.1016/0031-](https://doi.org/10.1016/0031-0182(94)90005-1)
1054 [0182\(94\)90005-1](https://doi.org/10.1016/0031-0182(94)90005-1).

1055 Sender, L.M., Villanueva-Amadoz, U., Pons, D., Diez, J.B., Ferrer, J., 2014. Singular
1056 taphonomic record of a wildfire event from middle Albian deposits of Escucha Formation
1057 in northeastern of Spain. *Hist. Biol.* 27(3–4), 442–452.
1058 <https://doi.org/10.1080/08912963.2014.895827>.

1059 Shao, L.Y., Wang, H., Yu, X.H., Lu, J., Zhang, M.Q., 2012. Paleo-fires and atmospheric oxygen
1060 levels in the latest Permian: evidence from maceral compositions of coals in Eastern
1061 Yunnan, Southern China. *Acta Geol. Sinica* 86(4), 949–962.

1062 Song, Z.H., 1986. Review on the study of early Cretaceous angiosperm pollen in China. *Acta*
1063 *Micropalaeontologica Sinica* 3(4), 373–380 (in Chinese with English abstract).

1064 Su, N., Zhu, G., Wu, X. D., Yin, H., Lu, Y.C., Zhang, S., 2021. Back-arc tectonic tempos:
1065 Records from Jurassic–Cretaceous basins in the eastern North China Craton. *Gondwana*
1066 *Res.* 90, 241–257. <https://doi.org/10.1016/j.gr.2020.12.002>.

1067 Sullivan, R.F., Boduszynski, M.M., Fetzer, J.C., 1989. Molecular transformations in
1068 hydrotreating and hydrocracking. *Energ. Fuel.* 3, 603–612.
1069 <https://doi.org/10.1021/ef00017a013>.

1070 Sun, G., Zheng, S.L., Sun, X.K., He, C.Q., Pu, T.Y., Shang, Y.K., Zhang, C.B., Yu, Z.Y.,
1071 Zhao, Y.H., 1992. Recent advance in the research of the strata near the Jurassic-Cretaceous
1072 boundary in eastern Heilongjiang. *J. Stratigr.* 16(1), 49–54 (in Chinese with English
1073 abstract).

1074 Sun, G., Dilcher, D.L., Zheng, S.L., Zhou, Z.K., 1998. In search of the first flower: a Jurassic
1075 angiosperm, *Archaeofructus*, from Northeast China. *Science* 282, 1692–1695.

1076 Sun, G., Ji, Q., Dilcher, D.L., Zheng, S.L., Nixon, K., Wang, X.F., 2002. *Archaeofructaceae*, a
1077 new basal angiosperm family. *Science* 296, 899–904.
1078 <https://doi.org/10.1126/science.1069439>.

1079 Sun, W. L. (2006). *China coalbed methane basins atlas*. Geological Publishing House, Beijing,

1080 pp. 1–233. (in Chinese).

1081 Sun, Y.W., Li, X., G.W., Liu, H., Zhang, Y.L., 2016. Aptian and Albian atmospheric CO₂
1082 changes during oceanic anoxic events Evidence from fossil *Ginkgo* cuticles in Jilin
1083 Province, Northeast China. *Cretaceous Res.* 62, 130–141.
1084 <https://doi.org/10.1016/j.cretres.2015.12.007>.

1085 Tao, M.H., Cui, Z.Q., Chen, G.Q., 2013. Mesozoic spore-pollen assemblages and climate
1086 fluctuations in northeastern China. *Acta Micropalaeontologica Sinica* 30(3), 275–287 (in
1087 Chinese with English abstract).

1088 Thompson, K.L., Picard, C.R., Chan, H.M., 2017. Polycyclic aromatic hydrocarbons (PAHs) in
1089 traditionally harvested bivalves in northern British Columbia, Canada. *Mar. Pollut. Bull.*
1090 121, 390–399. <https://doi.org/10.1016/j.marpolbul.2017.06.018>.

1091 Trabucho Alexandre, J., van Gilst, R.I., Rodríguez-López, J.P., De Boer, P.L., 2011. The
1092 sedimentary expression of oceanic anoxic event 1b in the North Atlantic. *Sedimentology*
1093 58, 1217–1246. <https://doi.org/10.1111/j.1365-3091.2010.01202.x>.

1094 Tsikos, H., Karakitsios, V., van Breugel, Y., Walsworth-Bell, B., Bombardiere, L., Petrizzo,
1095 M.R., Damst, J.S.S., Schouten, S., Erba, E., Silva, I.P., Farrimond, P., Tyson, R.V.,
1096 Jenkyns, H.C., 2004. Organic-carbon deposition in the Cretaceous of the Ionian Basin,
1097 NW Greece: the Paquier Event (OAE 1b) revisited. *Geol. Mag.* 141(4), 401–416.
1098 <http://dx.doi.org/10.1017/S0016756804009409>.

1099 Wan, X.Q., Li, G., Huang, Q.H., Xi, D.P., Chen, P.J., 2013. Division and correlation of
1100 terrestrial Cretaceous stages in China. *J. Stratigr.* 37(4), 457–471 (in Chinese with English
1101 abstract).

1102 Wang, W.F., Lu, S.K., Guo, Y.X., Sun, Y.P., 1998. Tectonic geometry and type of traps in
1103 Fuxin Basin. *J. Univ. Petrol. China* 22(3), 29–33 (in Chinese with English abstract).

1104 Wang, D.D., Yin, L.S., Shao, L.Y., Lv, D.W., Liu, H.Y., Wang, S., Dong, G.Q., 2021a.
1105 Characteristics and evolution of inertinite abundance and atmospheric *pO*₂ during China's
1106 coal-forming periods. *J. Palaeogeogr.* 10, 13. [https://doi.org/10.1186/s42501-021-00090-](https://doi.org/10.1186/s42501-021-00090-4)
1107 4.

1108 Wang, D.D., Mao, Q., Dong, G.Q., Yang, S.P., Lv, D.W., Yin, L.S., 2019a. The Primary
1109 investigation of the genetic mechanism of inertinite in the Middle Jurassic inertinite-rich

1110 coal seams of the southern Ordos Basin. *J. Geol. Res.* 1(3), 1–15.

1111 Wang, S., Shao, L.Y., Yan, Z.M., Shi, M.J., Zhang, Y.H., 2019b. Characteristics of Early
1112 Cretaceous wildfires in peat-forming environment, NE China. *J. Palaeogeogr.* 103(7),
1113 1653–1690. <https://doi.org/10.1186/s42501-019-0035-5>.

1114 Wang, S., Shao, L.Y., Li, J.X., Li, J.A., Jones, T., Zhu, M.Y., Zhou, J.M., 2021b. Coal
1115 petrology of the Yimin Formation (Albian) in the Hailar Basin, NE China:
1116 Paleoenvironments and wildfires during peat formation. *Cretaceous Res.* 124, 104815.
1117 <https://doi.org/10.1016/j.cretres.2021.104815>.

1118 Wildman, R.A., Hickey, L.J., Dickinson, M.B., Berner, R.A., Robinson, J.M., Dietrich, M.,
1119 Essenhight, R.H., Wildman, C.B., 2004. Burning of forest materials under late Paleozoic
1120 high atmospheric oxygen levels. *Geology*, 32(5), 457–460.
1121 <https://doi.org/10.1130/G20255.1>.

1122 Wu, F.Y., Xu, Y.G., Zhu, R.X., Zhang, G.W., 2014. Thinning and destruction of the cratonic
1123 lithosphere: a global perspective. *Sci. China Earth Sci.* 57 (2), 2878–2890.

1124 Xi, D.P., Wan, X.Q., Li, G.B., Li, G., 2019. Cretaceous integrative stratigraphy and timescale
1125 of China. *Sci. China Earth Sci.* 62(1), 256–286. [https://doi.org/10.1007/s11430-017-9262-](https://doi.org/10.1007/s11430-017-9262-y)
1126 [y](https://doi.org/10.1007/s11430-017-9262-y).

1127 Xu, D.B., Li, B.F., Chang, Z.L., Zhang, J.B., Cai, H.A., 2012. Study of U–Pb isotopic age and
1128 sequence of the Cretaceous volcanic rocks and coal-searching in Fuxian–Zhangwu–
1129 Heishan area, western Liaoning Province. *Earth Sci. Front.* 19 (6), 155–166 (in Chinese
1130 with English abstract).

1131 Xu, X.T., Shao, L.Y., 2018. Limiting factors in utilization of chemical index of alteration of
1132 mudstones to quantify the degree of weathering in provenance. *J. Palaeogeogr.* 20(3), 515–
1133 522. (in Chinese with English abstract).

1134 Xu, X.T., Shao, L.Y., Lan, B., Wang, S., Hilton, J., Qin, J., Hou, H., Zhao, J., 2020a.
1135 Continental chemical weathering during the Early Cretaceous Oceanic Anoxic Event (OAE
1136 1b): a case study from the Fuxin fluvio-lacustrine basin, Liaoning Province, NE China. *J.*
1137 *Palaeogeogr.* 9(2), 246–266. <https://doi.org/10.1186/s42501-020-00056-y>.

1138 Xu, X.T., Shao, L.Y., Fu, Y.F., Wang, D.D., Cai, H.A., Qin, J.Y., Hou, H.H., Zhao, J., 2020b.
1139 Sequence palaeogeography, lacustrine basin evolution, and coal accumulation in the Lower

- 1140 Cretaceous Fuxin continental faulted basin, China. *Geol. J.* 55(2), 1195–1215.
1141 <https://doi.org/10.1002/gj.3483>.
- 1142 Xu, X.T., Shao, L.Y., Eriksson, K.A., Pang, B., Wang, S., Yang, C.X., Hou, H.H., 2022.
1143 Terrestrial records of the early Albian Ocean Anoxic Event: Evidence from the Fuxin
1144 lacustrine basin, NE China. *Geosci. Front.* 13(1), 101275.
1145 <https://doi.org/10.1016/j.gsf.2021.101275>.
- 1146 Xu, Y., Uhl, D., Zhang, N., Zhao, C., Qin, S., Liang, H., Sun, Y., 2020c. Evidence of
1147 widespread wildfires in coal seams from the Middle Jurassic of Northwest China and its
1148 impact on paleoclimate. *Palaeogeogr. Palaeoclimatol. Palaeoecol.* 559, 109819.
1149 <https://doi.org/10.1016/j.palaeo.2020.109819>.
- 1150 Yan, Z.M., Shao, L.Y., Glasspool, I.J., Wang, J., Wang, X.T., Wang, H., 2019. Frequent and
1151 intense fires in the final coals of the Paleozoic indicate elevated atmospheric oxygen
1152 levels at the onset of the End-Permian Mass Extinction Event. *Int. J. Coal Geol.* 207, 75–
1153 83. <https://doi.org/10.1016/j.coal.2019.03.016>.
- 1154 Yang, Y.K., 1996. Atlas for Coal Petrography of China. China University of Mining and
1155 Technology Press, Xuzhou, pp. 1–99. (in Chinese).
- 1156 Zakir Hossain, H.M., Sampei, Y., Roser, B.P., 2013. Polycyclic aromatic hydrocarbons (PAHs)
1157 in late Eocene to early Pleistocene mudstones of the Sylhet succession, NE Bengal Basin,
1158 Bangladesh: Implications for source and paleoclimate conditions during Himalayan uplift.
1159 *Org. Geochem.* 56, 25–39. <https://doi.org/10.1016/j.orggeochem.2012.12.001>.
- 1160 Zhang, J., 2003. Geothermal resources hosting condition analysis, Dongliang District, Fuxin
1161 Basin. *Coal Geol. China* 15(6), 37–39. (in Chinese with English abstract).
- 1162 Zhang, Q., Zhang, M.S., Li, X.B., Wang, Y.N., Liu, X.S., Zhang, M.M., 2016. Stratigraphic
1163 sequences and zircon U–Pb dating of Yixian Formation in Caozhuang area of Xingcheng,
1164 western Liaoning. *Global Geol.* 35(1), 51–65. (in Chinese with English abstract).
- 1165 Zhang, Z.H., Wang, C.S., Lv, D.W., Hayd, W.W., Wang, T.T., Cao, S., 2020. Precession-scale
1166 climate forcing of peatland wildfires during the early middle Jurassic greenhouse period.
1167 *Glob. Planet. Chang.* 184, 103051. <https://doi.org/10.1016/j.gloplacha.2019.103051>.
- 1168 Zhao, X.D., Zheng, D.R., Wang, H., Fang, Y.N., Xue, N.H., Zhang, H.C., 2022. Carbon cycle
1169 perturbation and mercury anomalies in terrestrial Oceanic Anoxic Event 1b from Jiuquan

- 1170 Basin, NW China. Geological Society, London, Special Publications 521.
- 1171 Zhou, W.F., Algeo, T.J., Luo, G.M., Ruan, X.Y., Chen, Z.Q., Xie, S.C., 2021. Hydrocarbon
1172 compound evidence in marine successions of South China for frequent wildfires during the
1173 Permian-Triassic transition. *Glob. Planet. Chang.* 200, 103472.
1174 <https://doi.org/10.1016/j.gloplacha.2021.103472>.
- 1175 Zhou, Z.H., Barrett, P.M., Hilton, J., 2003. An exceptionally preserved Lower Cretaceous
1176 ecosystem. *Nature* 421, 807–814. <https://doi.org/10.1038/nature01420>.
- 1177 Zhu, R.X., Lo, C.H., Shi, R.P., Shi, G.G., Pan, Y.X., Sha, J., 2004. Palaeointensities determined
1178 from the middle Cretaceous basalt in Liaoning Province, northeastern China. *Phys. Earth
1179 Planet. In.* 142, 49–59. <https://doi.org/10.1016/j.pepi.2003.12.013>.
- 1180 Zhu, R.X., Zhang, H.F., Zhu, G., Meng, Q.R., Fan, H.R., Yang, J.H., Wu, F.Y., Zhang, Z.Y.,
1181 Zheng, T.Y., 2017. Craton destruction and related resources. *Int. J. Earth Sci.* 106, 2233–
1182 2257.
- 1183 Zhu, Z.M., Yan, J.F., Shen, B., Zhou, J.Y., 2007. Co-existing formation of multi-energy
1184 resources in the Fuxin Basin analysis from tectonic-thermal events. *Adv. Earth Sci.* 22(5),
1185 468–479. (in Chinese with English abstract).

1186

1187 **Figures and table captions**

1188 Fig. 1. Location of the Fuxin Basin. a. Outline map of China showing position of Fuxin Basin.
1189 b. Enlargement of the top right part of Figure 1a showing position of the Fuxin basin and
1190 tectonic features (modified after Zhu et al., 2007). c. Global palaeogeographic map of the early
1191 Cretaceous showing approximate location of study area (modified from the ~110 Ma map of
1192 the webpage <https://deeptimemaps.com/global-paleogeography-and-tectonics-in-deep-time>).
1193 Abbreviations: AfP = African Plate; AnP = Antarctic Plate; Arp = Arabian Plate; AuP =
1194 Australian Plate; CAP = Central Asian Plate; EP = European Plate; IP = Indian Plate; NAP =
1195 North America Plate; NCP = North China Plate; SAmP = South American Plate; SAsP =
1196 Southeast Asian Plate; SCP = South China Plate; SP = Siberian Plate.

1197

1198 Fig. 2. Geology and stratigraphy of the Fuxin Basin. a. Geologic map of the Fuxin Basin
1199 (modified after Sun, 2006); cross-section A-A' is modified from the interpreted seismic profile

1200 (Zhu et al., 2007; Su et al., 2021). b. Stratigraphic succession for the western Liaoning region
1201 during the Aptian–Albian interval with flora assemblages (Deng et al., 2012) and isotopic ages.
1202 Age sources: ① from Zhang et al. 2016; ② from Xu et al. 2012; ③ from Su et al. 2021; ④
1203 from He et al. 2004; ⑤ from Xu et al. 2021; ⑥ from Zhu et al. 2004. I, II, III and IV represent
1204 the first, second, third and fourth members of the Shahai Formation, respectively.

1205 Abbreviations: Flora assem. = Flora assemblages.

1206

1207 Fig. 3. Stratigraphic distribution of kerogen macerals from mudstone samples in borehole DY-1
1208 from the Lower Cretaceous Shahai and Fuxin formations in the Fuxin Basin. The interpretation
1209 of the sedimentary environments and zircon U-Pb age is from Xu et al. (2022). Abbreviations:

1210 J. F. = Jiufotang Formation; S. F. = Sunjiawan Formation; Sed. en. = Sedimentary

1211 environments.

1212

1213 Fig. 4. Photomicrographs showing microstructural characteristics of kerogen macerals from
1214 borehole DY-1 in the early Cretaceous Fuxin Basin. a and b, sapropelinite (transmitted light,
1215 600m and 1095.5m). c and d, vitrinite (transmitted light, 714.5m). e and f, conifer pollen
1216 (transmitted light and fluorescence, respectively, 714.5m). g. fern spore (transmitted light,
1217 714.5m). h. conifer pollen (transmitted light, 413m). i. conifer pollen (transmitted light,
1218 714.5m). j. conifer pollen (transmitted light, 856m). k, l and m, inertinite (transmitted light,
1219 413m, 1146m and 946.3m).

1220

1221 Fig. 5. Photographs of macroscopic charcoal and plant fossils from borehole DY-1 and
1222 outcrops in the early Cretaceous Fuxin Basin. a. Small charcoal fragments with black color in
1223 sandstone, 541m. b. Charcoalified wood fragments in mudstone, 625.8m. c. Small charcoals
1224 showing long strips in fine sandstone, 847.5m. d-f. Lacustrine mudstone with abundant charred
1225 plant fossil fragments, the depth is 862.2m, 919.8m and 920.5m respectively. g. Small
1226 charcoalified wood fragments in lacustrine mudstone, 1093.8m. h. Charred tree trunk fossil in
1227 lacustrine mudstone, 1135.9m. i. Charcoalified tree trunk fossil and angular wood fragments
1228 Haizhou open-pit coal mine section; the hammer is 30 cm long. j. Abundant charcoal fragments
1229 in sandstones showing cubic blocks of charcoalified wood, Haizhou open-pit coal mine
1230 section; the hammer is 30 cm long. k. Grey mudstone with cycad fossil fragments, 540m. l.

1231 Grey siltstone with cycad fossil fragments, Haizhou open-pit coal mine section.

1232

1233 Fig. 6. Photomicrographs of inertinite contents in mudstone from borehole DY-1 in the early
1234 Cretaceous Fuxin Basin. a. Inertinite with compressed and broken cell walls, reflected light,
1235 413m. b and c, inertinite, reflected light, 459m and 800m. d. Inertinite with regular and
1236 complete arrangement of cellular structure with relatively high reflectance, 1095.5m.

1237

1238 Fig. 7. Scanning electron micrographs of inertinite in mudstone from borehole DY-1; early
1239 Cretaceous Fuxin Basin. a. Detail of tracheids with uniseriate, contiguous, circular pits in
1240 walls, 458.6m. b. Longitudinal section of tracheids showing homogenized cell walls, 625.8m.
1241 c. Transverse section of vessels with high density, 847.5m. d. Longitudinal section of tracheids
1242 with tracheids broken by compaction, 868.9m. e. Cross-section with homogenized cell walls,
1243 919.8m. f. Cross-section showing relatively well-preserved tracheids with cellular structure,
1244 1093.8m.

1245

1246 Fig. 8. Total ion current traces of aromatic hydrocarbon fractions for the ten mudstone samples
1247 in borehole DY-1 from the early Cretaceous Fuxin Basin. Structures for selected PAHs show
1248 the total ion current chromatograms of samples DY-1-5, DY-1-8 and DY-1-16. IS-internal
1249 standard; VI-Phenanthrene; VII-Anthracene; VIII-Retene; IX-Fluoranthene; X-
1250 Benzo[a]fluorine; XI-Benzo[b]fluorine; XII-Pyrene; XIII-Benz(a)anthracene; XIV- Chrysene;
1251 XV-Benzofluorathenes; XVI-Benzo(e)pyrene; XVII-Benzo(a)pyrene; XVIII-Perylene.

1252

1253 Fig. 9. Carbon isotopic correlation of the OAE1b event between marine and terrestrial
1254 successions. Carbon isotopic data collected from the borehole DY-1 in the Fuxin Basin, NE
1255 China. Data collated for the Fuxin terrestrial basin from Xu et al. (2022), the Chong'an
1256 terrestrial section in SE China from Hu et al. (2014), the Hanxiagou terrestrial section in NW
1257 China from Zhao et al. (2022), the marine Vocontian Basin (SE France) from Herrle et al.
1258 (2004), the marine Poggio le Guaine Section from Matsumoto et al. (2020), the marine Andean
1259 Basin, northern Peru from Navarro-Ramirez et al. (2015) and ODP site 1049 off northern
1260 Florida on the Blake Nose escarpment from Huber et al. (2011).

1261

1262 Fig. 10. Correlation of kerogen macerals, wildfire types, organic carbon isotopes ($\delta^{13}\text{C}_{\text{org}}$) and
1263 total organic carbon (TOC) across the early Albian OAE 1b. Depth locations are shown in Fig.
1264 4. The zircon U-Pb age, organic carbon isotopes ($\delta^{13}\text{C}_{\text{org}}$) and total organic carbon (TOC) is
1265 from Xu et al. (2022). Abbreviations: J. F. = Jiufotang Formation; S. F. = Sunjiawan Formation.
1266

1267 Fig. 11. Predictions of $p\text{O}_2$ in Unit C during the early Albian in the Fuxin Basin based on the
1268 model proposed by Glasspool et al. (2015). S-shaped curves are assumed to ensure a smooth
1269 transition from 0% inertinite at low oxygen levels to 100% inertinite at high oxygen levels.
1270 However, the curve above 35% $p\text{O}_2$ is relatively unimportant as plant biomass can still burn so
1271 readily as to be incompatible with sustained plant growth (Jones and Chaloner, 1991). The two
1272 blue curves represent the error interval. Red curve represents the best estimate for $p\text{O}_2$ level.
1273 Abbreviations: Min. = minimum; Max. = maximum; Aver. = average.

1274

1275 Fig. 12. Schematic model illustrating possible relationship between wildfire activity and anoxia
1276 in the Fuxin lacustrine basin during the early Albian OAE 1b. Wildfires and associated post-
1277 fire erosion intensified the transport rate of nutrients and organic matter from continents into
1278 lakes under conditions of intensified continental chemical weathering, thereby contributing to
1279 eutrophication and anoxia in lacustrine and contemporaneous oceanic systems.

1280

1281 Table 1 Kerogen macerals and inertinite reflectance values of mudstone samples from the
1282 Lower Cretaceous Shaihai and Fuxin formations in the Fuxin Basin.

1283

1284 Table 2 Concentration of the PAHs of ten mudstones from the early Cretaceous Fuxin Basin.

1285

Fig. 1

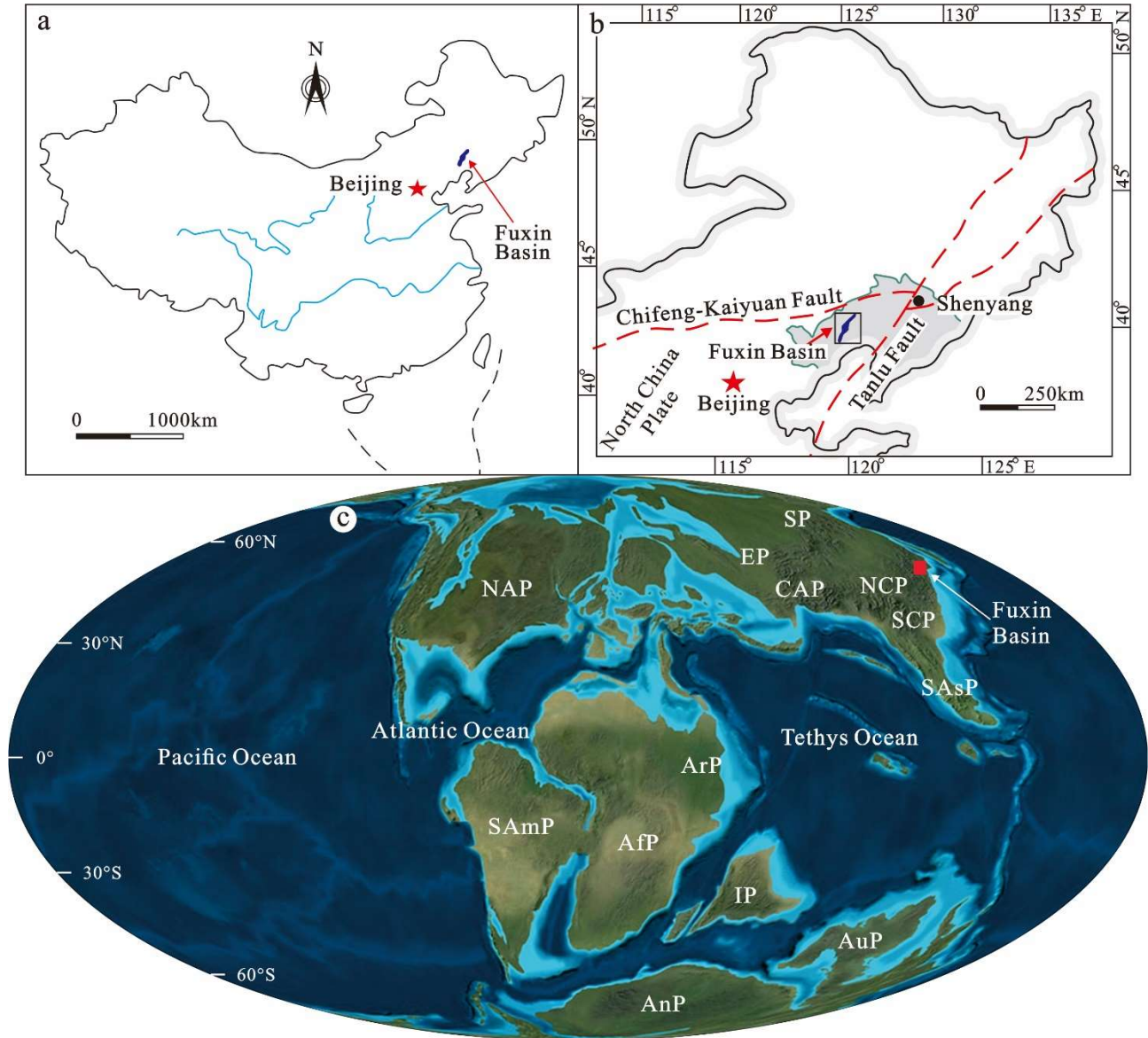


Fig. 2

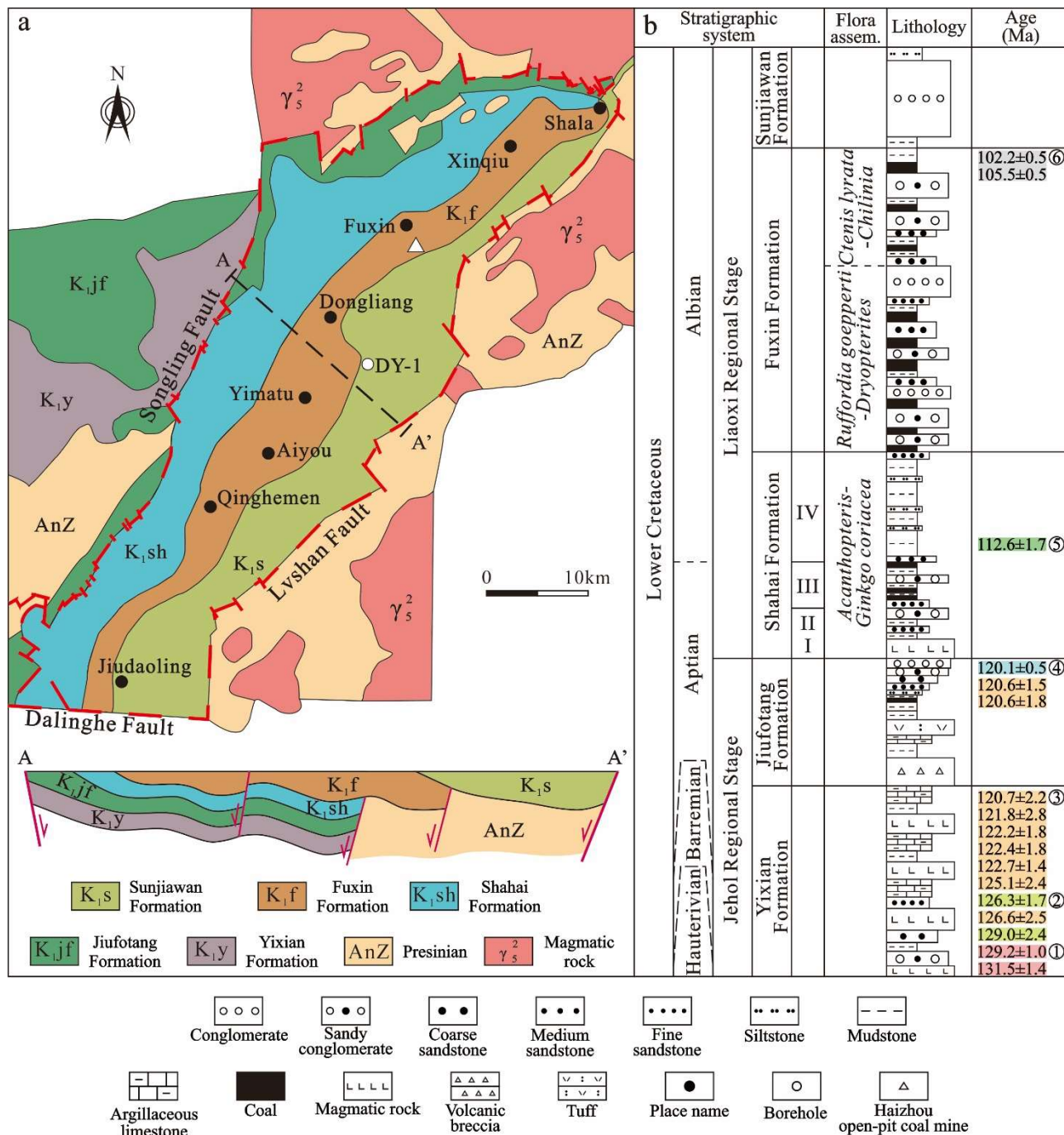


Fig. 3

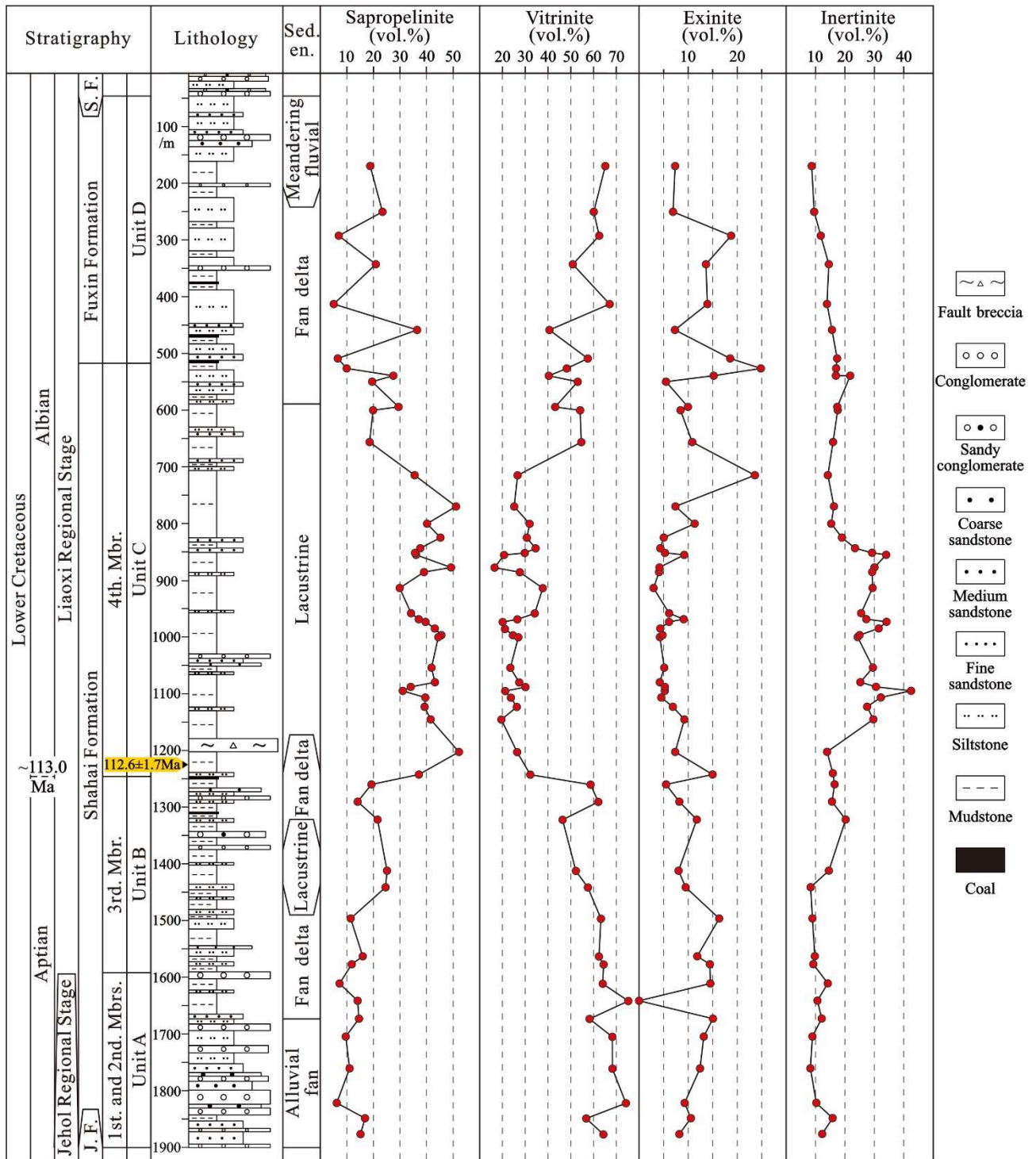


Fig. 4

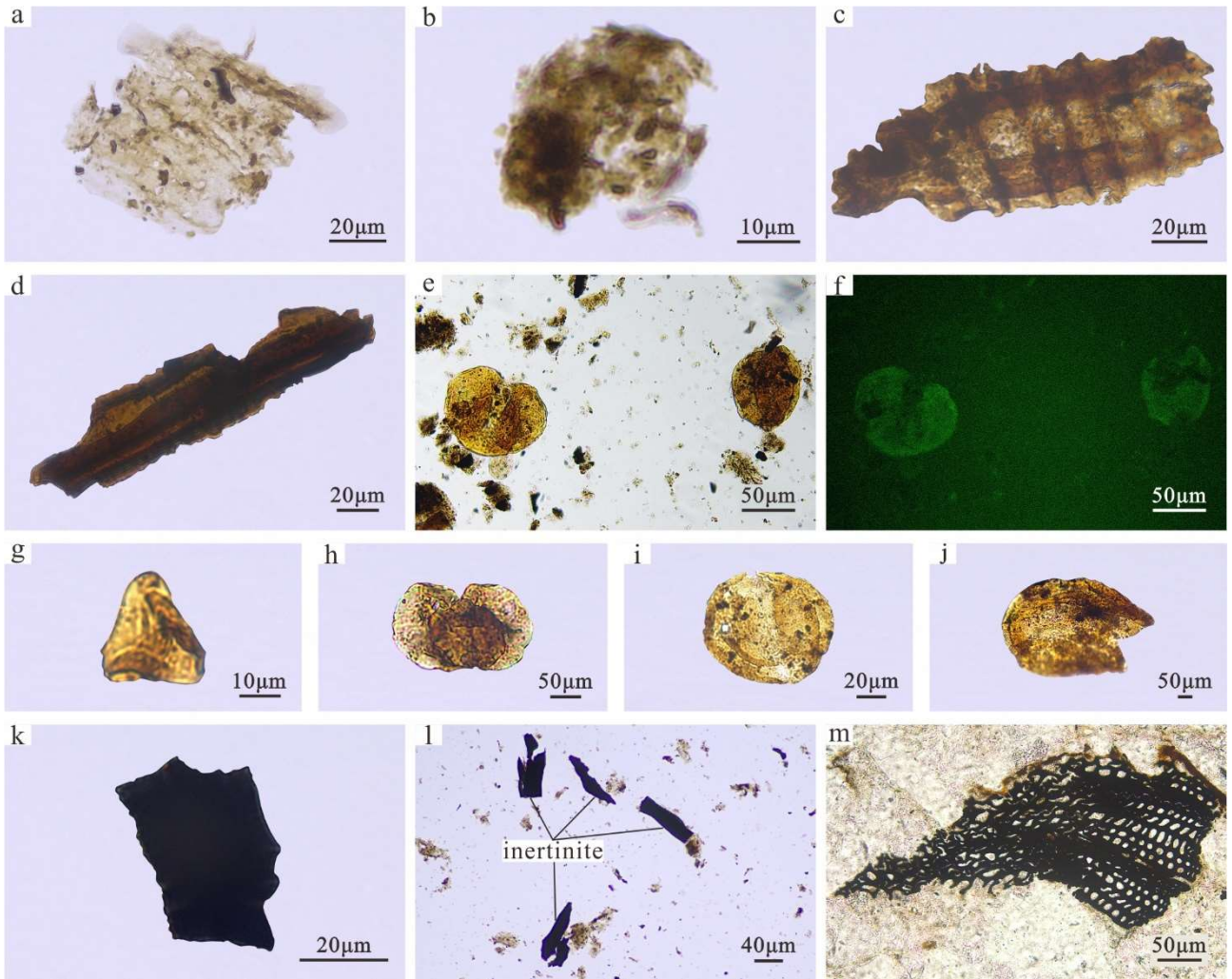


Fig. 5

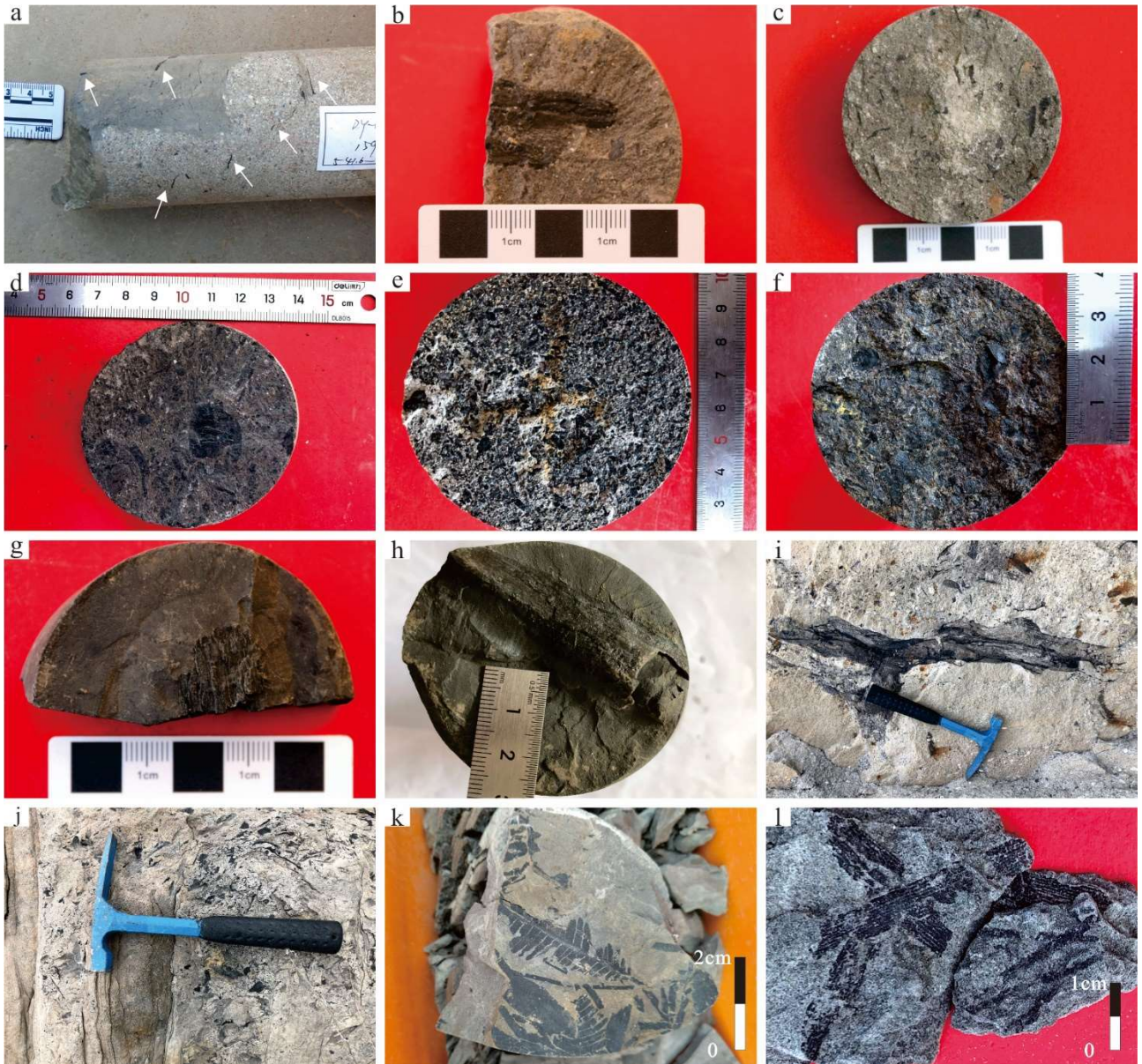


Fig. 6

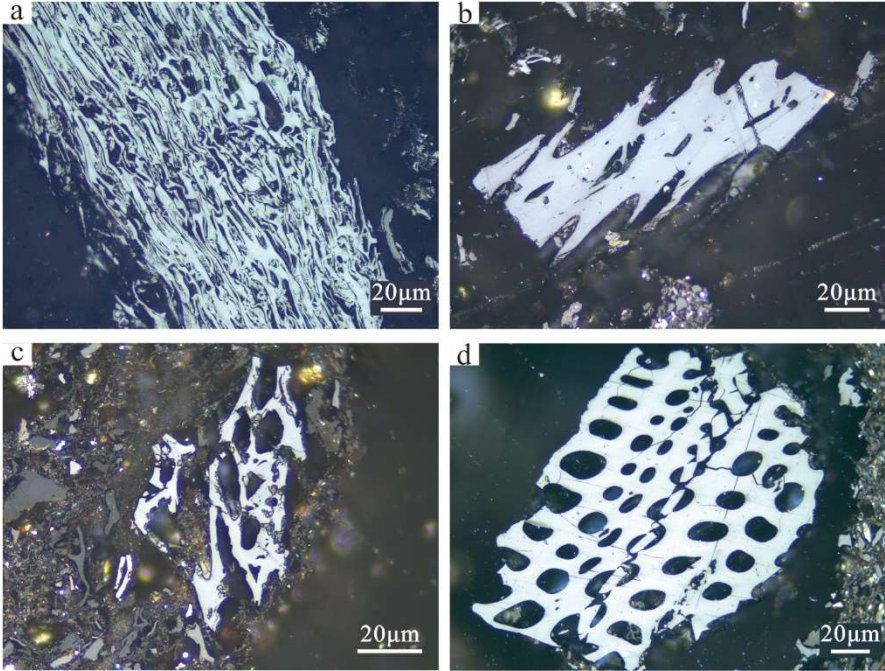


Fig. 7

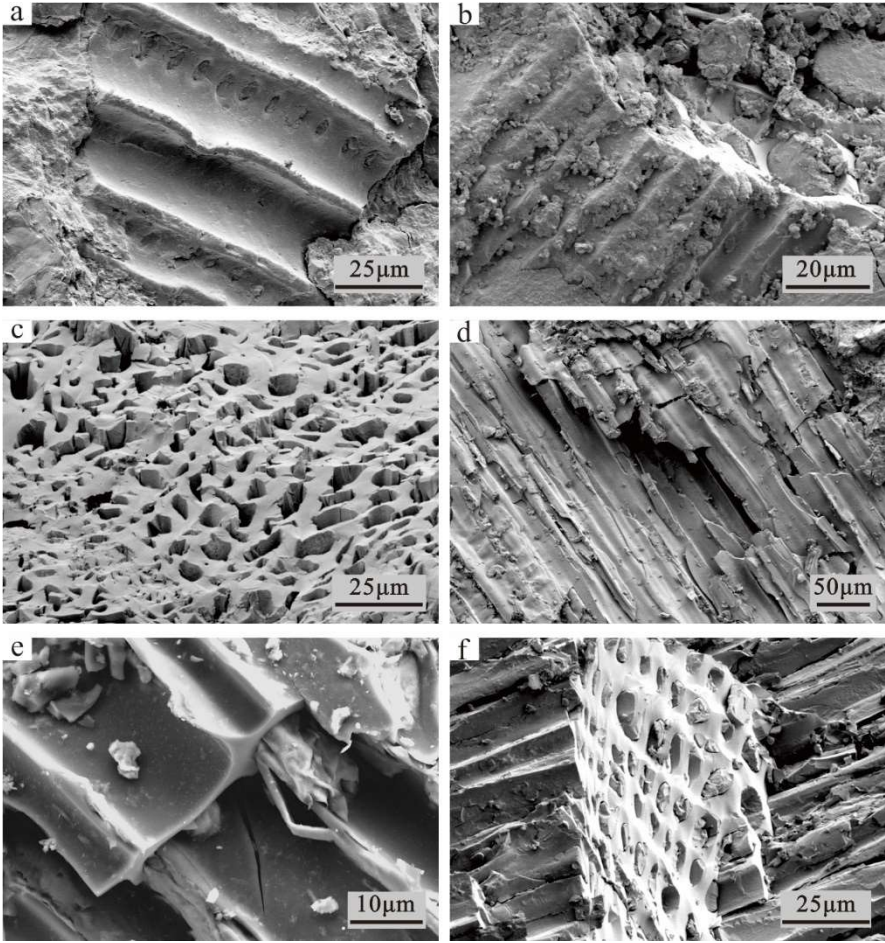


Fig. 8

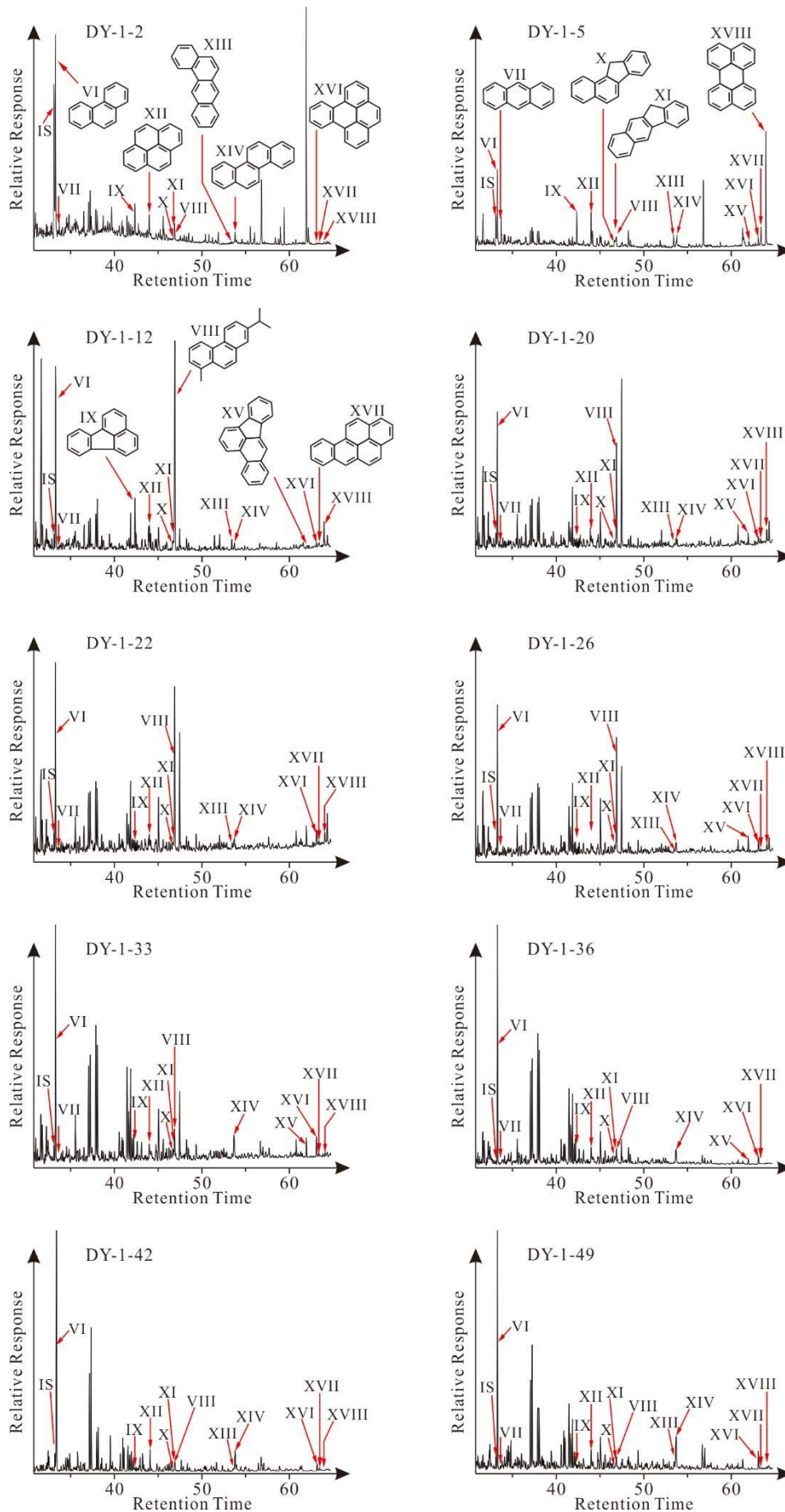


Fig. 9

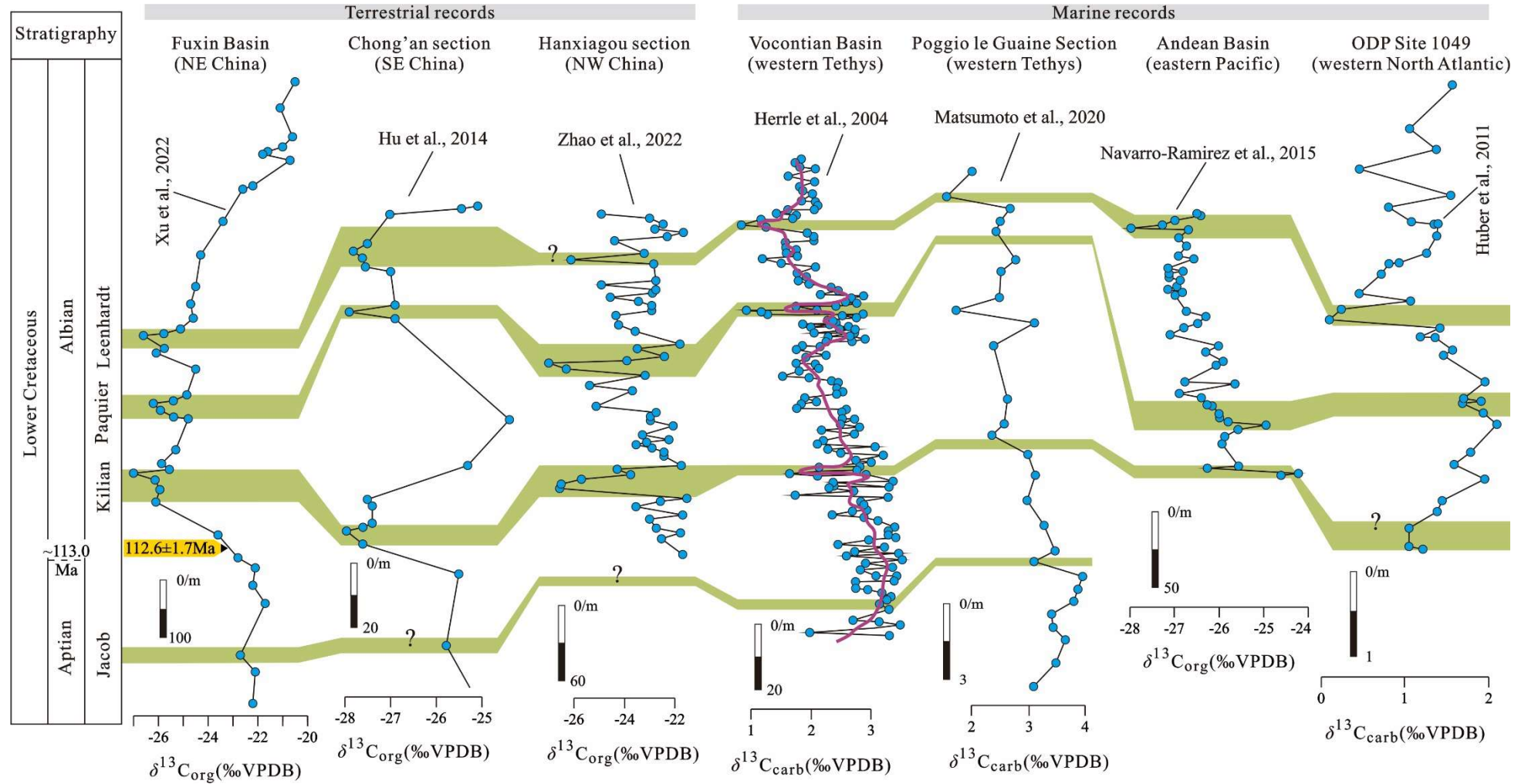


Fig. 10

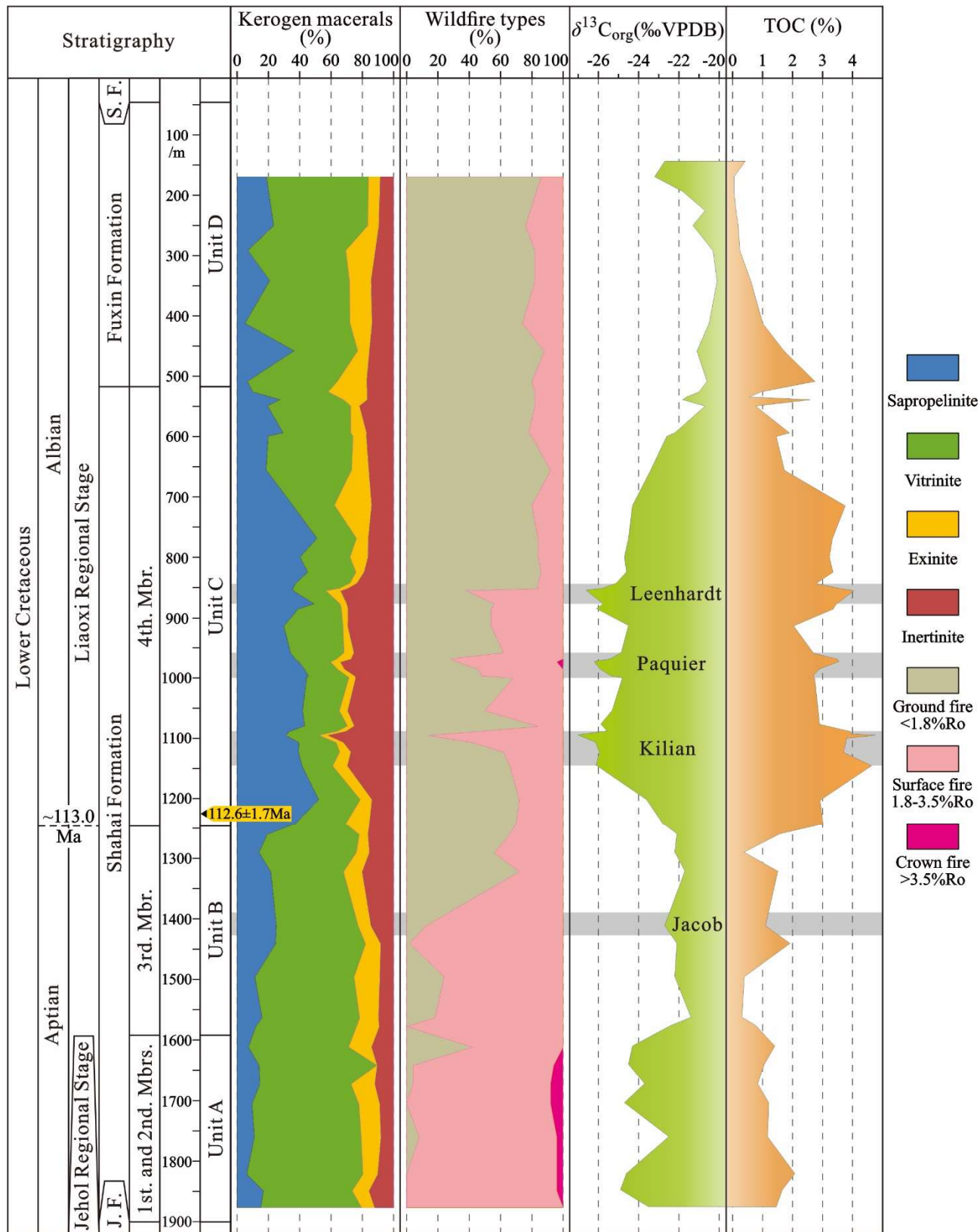


Fig. 11

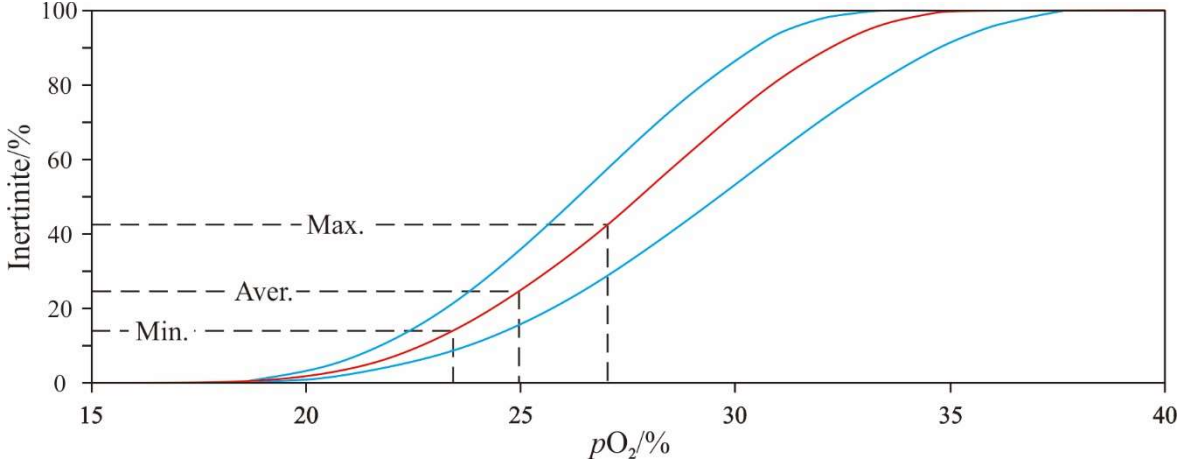


Fig. 12

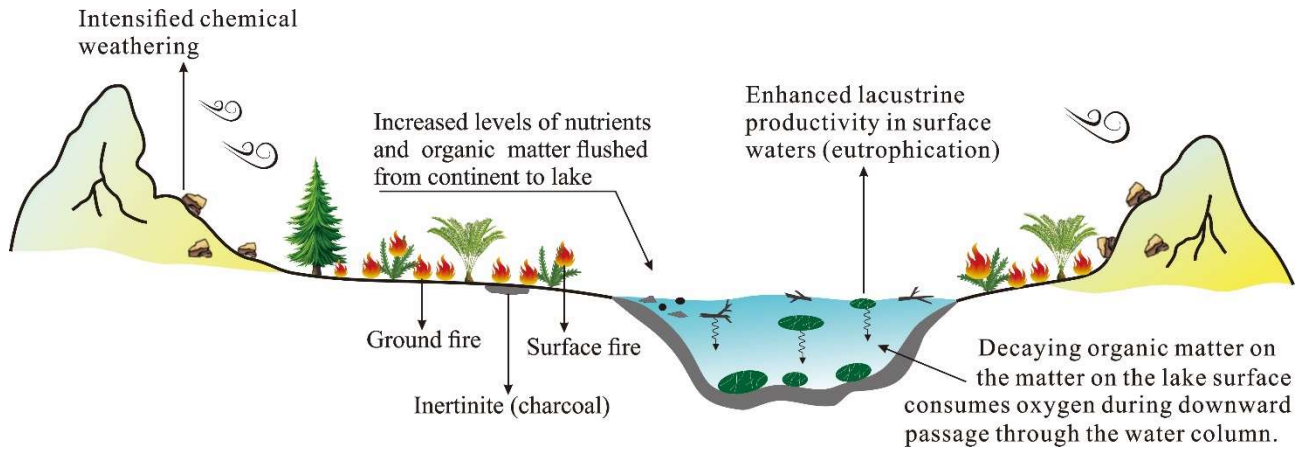


Table 1

Organic carbon isotope ($\delta^{13}\text{C}_{\text{org}}$), total organic carbon (TOC), kerogen macerals and inertinite reflectance values of mudstone samples from the Lower Cretaceous Shahai and Fuxin formations in the Fuxin Basin.

Borehole	Sample	Depth/m	$\delta^{13}\text{C}_{\text{org}}$	TOC	Kerogen macerals (vol.%, mmf)				Inertinite reflectance (%Ro)		
			‰VPD	%	Sap.	Vitr.	Exi.	Iner.	Min.	Max.	Aver.
	DY-1-1	144	-22.7	0.42	-	-	-	-	-	-	-
	DY-1-2	170	-23.2	0.05	18.8	65.1	7.3	8.7	0.9	2.4	1.4
	DY-1-3	194.6	-21.8	0.05	-	-	-	-	-	-	-
	DY-1-4	225.5	-20.7	0.12	-	-	-	-	-	-	-
	DY-1-5	251	-21.3	0.19	23.4	60.1	6.9	9.6	1.2	2.1	1.7
	DY-1-6	292.6	-20.3	0.25	6.9	62.5	18.8	11.8	0.8	2.2	1.4
	DY-1-7	342.7	-20.1	0.61	20.9	50.9	13.6	14.5	0.9	2.2	1.4
	DY-1-8	413	-20.5	1.01	5.1	67.1	13.9	13.9	1.0	2.5	1.6
	DY-1-9	459	-21.1	1.72	36.5	40.6	7.3	15.6	1.1	2.3	1.6
	DY-1-10	509.5	-20.6	2.75	6.6	57.5	18.6	17.4	0.9	2.6	1.6
	DY-1-11	527	-21.0	0.93	9.9	48.2	24.8	17.0	1.1	2.1	1.6
	DY-1-12	535	-21.6	0.57	-	-	-	-	-	-	-
	DY-1-13	540	-21.8	2.59	27.5	40.4	15.2	17.0	0.6	2.0	1.3
	DY-1-14	549.5	-20.7	0.77	19.5	53.0	5.5	22.0	0.9	2.0	1.4
	DY-1-15	594.5	-22.2	1.90	29.5	43.2	10.0	17.4	0.8	2.4	1.5
	DY-1-16	600	-22.6	1.46	19.9	54.1	8.4	17.5	0.8	2.1	1.4
	DY-1-17	656	-23.4	1.73	18.6	54.6	10.8	16.0	1.0	2.0	1.4
	DY-1-18	714.5	-24.3	3.76	35.5	26.6	23.6	14.2	0.8	2.1	1.4
	DY-1-19	769.5	-24.5	3.33	51.1	25.2	7.4	16.3	0.8	2.3	1.6
	DY-1-20	800	-24.7	3.23	40.2	32.0	11.3	16.5	1.1	2.3	1.5
	DY-1-21	824.9	-24.6	3.34	45.3	30.7	5.0	19.0	1.1	2.4	1.5
	DY-1-22	843.3	-25.1	2.79	37.7	34.6	4.3	23.5	0.9	2.2	1.5
	DY-1-23	852.2	-25.8	3.65	35.7	29.8	5.3	29.2	1.2	2.7	1.6
	DY-1-24	856	-26.6	4.05	36.1	20.7	9.2	34.0	1.5	2.9	1.9
	DY-1-25	877.7	-25.7	3.45	49.2	16.6	4.1	30.1	1.4	2.5	1.8
	DY-1-26	886	-26.1	3.36	39.0	27.6	4.1	29.3	1.2	2.8	1.8
	DY-1-27	914.5	-24.5	2.04	29.9	37.7	2.9	29.4	1.1	2.4	1.8
	DY-1-28	958.5	-24.9	2.70	34.2	34.2	6.1	25.5	1.2	2.9	1.8
	DY-1-29	968.6	-25.4	3.49	37.1	26.6	9.1	27.3	1.0	2.9	2.1
	DY-1-30	974	-26.2	3.55	39.6	20.1	6.1	34.1	1.2	3.8	2.3
	DY-1-31	985.9	-25.9	2.89	43.1	21.1	4.3	31.5	1.2	2.8	1.9
	DY-1-32	997	-25.4	2.69	45.6	24.6	4.8	25.0	1.3	2.9	1.8
	DY-1-33	1000	-24.8	2.74	44.4	27.0	4.2	24.3	0.9	2.5	1.8
	DY-1-34	1055	-25.3	2.86	41.9	23.5	5.1	29.5	0.9	2.6	1.8
	DY-1-35	1080.4	-25.9	2.90	43.2	27.4	4.2	25.3	1.3	2.4	1.7
	DY-1-36	1088.3	-25.6	3.92	34.1	30.1	5.2	30.6	1.0	3.0	1.8
	DY-1-37	1095.5	-27.0	4.76	31.0	21.2	5.2	42.5	1.7	3.3	2.3
	DY-1-38	1107.5	-26.1	3.78	39.5	23.7	4.5	32.2	1.4	3.0	2.1
	DY-1-39	1123.3	-25.9	3.70	39.3	26.3	6.9	27.5	1.3	2.6	1.8

DY-1-40	1146	-26.1	4.64	41.5	19.6	9.2	29.7	1.1	3.0	1.8
DY-1-41	1202.5	-23.6	2.92	52.2	26.5	7.4	14.0	1.3	2.3	1.7
DY-1-42	1242.3	-22.8	3.02	37.1	32.2	15.0	15.6	1.3	2.3	1.7
DY-1-43	1260.4	-22.1	1.58	19.3	58.7	5.5	16.5	1.1	2.8	1.8
DY-1-44	1291.2	-22.2	0.38	14.1	62.1	8.2	15.6	0.8	2.6	1.8
DY-1-45	1322.3	-21.7	1.51	21.6	46.4	11.8	20.3	0.8	2.6	1.6
DY-1-46	1412.5	-22.7	1.10	25.1	52.3	8.0	14.6	1.6	3.4	2.2
DY-1-47	1441.2	-22.1	1.92	24.6	57.5	9.5	8.4	1.8	3.4	2.6
DY-1-48	1496.3	-22.2	0.40	11.4	63.3	16.3	9.0	0.8	3.3	2.0
DY-1-49	1563.8	-21.4	0.32	16.0	62.4	11.9	9.8	1.0	3.3	2.2
DY-1-50	1578	-22.4	0.78	11.9	64.4	14.4	9.3	1.8	3.1	2.4
DY-1-51	1612	-24.3	1.41	7.3	64.0	14.5	14.2	1.0	3.0	1.9
DY-1-52	1642	-24.5	1.06	14.0	75.3	0.0	10.7	1.6	4.3	2.6
DY-1-53	1673.3	-23.7	0.84	14.6	58.3	15.0	12.1	1.8	3.8	2.6
DY-1-54	1705.3	-24.7	1.21	9.6	68.3	13.2	9.0	2.0	3.7	2.8
DY-1-55	1761	-22.5	1.17	11.0	68.3	12.4	8.3	1.7	3.6	2.5
DY-1-56	1821.6	-24.6	2.08	6.2	74.2	9.3	10.3	1.8	4.1	2.6
DY-1-57	1849.3	-24.9	1.66	16.8	56.8	10.6	15.8	1.8	3.6	2.4
DY-1-58	1876.8	-23.5	1.46	15.2	64.3	8.2	12.3	2.0	3.2	2.6

Abbreviations: Iner. = inertinite; Vitr. = vitrinite; Exi. = exinite; Sap. = sapropelite. Min. = minimum; Max. = maximum; Aver. = average; mmf = mineral matter free.

Table 2

Concentration of the PAHs of ten mudstones from the early Cretaceous Fuxin Basin.

Number	Compound name	Sample number / Concentration of PAHs ($\mu\text{g/g}$ mudstone)									
		DY-1-5	DY-1-8	DY-1-16	DY-1-24	DY-1-26	DY-1-30	DY-1-37	DY-1-40	DY-1-46	DY-1-53
IS	D10-Phenanthrene	0.04141	0.04515	0.02849	0.11199	0.07819	0.07426	0.14018	0.04184	0.15060	0.03929
I	Naphthalene	0.00001	0	0	0	0	0.00399	0	0.00147	0	0
II	Fluorene	0.00061	0.00350	0.01169	0.02711	0.02077	0.03674	0.03862	0.04673	0.03681	0.05182
III	Biphenyl	0.00001	0	0.00294	0.01860	0.00612	0.04734	0.01910	0.09328	0	0.00508
IV	Dibenzothiophene	0.00216	0.00575	0.01254	0.03321	0.03150	0.07033	0.08076	0.11306	0.17462	0.05195
V	Dibenzofuran	0.00037	0.00815	0.09972	0.26086	0.12739	0.29177	0.17239	0.23040	0.00313	0.03044
VI	Phenanthrene	0.05655	0.12072	0.33174	0.88579	0.67586	1.31083	2.03635	2.72338	2.20779	0.75873
VII	Anthracene	0.00110	0.00300	0.00225	0.00275	0.00440	0.00368	0.00166	0.00436	0	0.00913
VIII	Retene	0.00158	0.00423	0.12800	0.21727	0.18751	0.30194	0.08485	0.04924	0.00130	0.01169
IX	Fluoranthene	0.00917	0.05118	0.09612	0.05740	0.03818	0.05019	0.03035	0.03064	0.04148	0.01406
X	Benzo[a]fluorene	0.00021	0.00340	0.00422	0.00493	0.00374	0.00598	0.00618	0.00597	0.00844	0.00160
XI	Benzo[b]fluorene	0.00068	0.01587	0.02661	0.05715	0.04476	0.07620	0.06073	0.05725	0.06277	0.01849
XII	Pyrene	0.00695	0.05776	0.04693	0.07843	0.06009	0.09071	0.13335	0.17908	0.19042	0.06031
XIII	Benz(a)anthracene	0.00027	0.01811	0.01818	0.00485	0.00324	0.00216	0	0	0.00718	0.00259
XIV	Chrysene	0.00044	0.01326	0.01484	0.05154	0.04669	0.10972	0.23315	0.21152	0.24639	0.12779
XV	Benzo[fluoranthenes	0	0.00264	0.00134	0.00363	0	0.00624	0.00853	0.00319	0	0
XVI	Benzo(e)pyrene	0.00040	0.01185	0.00659	0.04256	0.04892	0.08219	0.15981	0.09193	0.06859	0.05603
XVII	Benzo(a)pyrene	0.00037	0.02997	0.00485	0.00733	0.00671	0.00775	0.00714	0.00426	0.00550	0.00197
XVIII	Perylene	0.00053	0.18778	0.04626	0.00069	0.00032	0.00076	0.00179	0	0.00028	0.00049
Total PAHs (more than 3-ring)		0.07825	0.51976	0.72792	1.41431	1.12043	2.04836	2.76389	3.36081	2.84014	1.06287